Monthly Notices of the ROYAL ASTRONOMICAL SOCIETY

MNRAS **544,** 1038–1055 (2025) https://doi.org/10.1093/mnras/staf1760
Advance Access publication 2025 October 14

High-order stellar kinematics in MaNGA integral-field spectroscopy survey: classification, stellar population, and the impact of galaxy bars and mergers

Youquan Fu [1]★ Michele Cappellari [2] Kai Zhu [1] Shude Mao [3] and Shengdong Lu [4]

[1]*Department of Astronomy, Tsinghua University, Beijing 100084, China*
[2]*Sub-Department of Astrophysics, Department of Physics, University of Oxford, Denys Wilkinson Building, Keble Road, Oxford OX1 3RH, UK*
[3]*Department of Astronomy, Westlake University, Hangzhou 310030, Zhejiang Province, China*
[4]*Institute for Computational Cosmology, Department of Physics, University of Durham, South Road, Durham DH1 3LE, UK*

Accepted 2025 October 5. Received 2025 September 23; in original form 2025 January 12

ABSTRACT

We extract with PPXF and analyse the high-order stellar kinematic moments h_3 (related to skewness) and h_4 (related to kurtosis) in a complete subsample of 2230 galaxies with well-sampled line-of-sight velocity distributions ($\sigma_e \gtrsim 140\,\mathrm{km\,s^{-1}}$) from the final data release of 10 010 unique galaxies of the MaNGA survey. To reduce template mismatch, we created a stellar library based on MaStar. We used proxies for the specific angular momentum parameter (λ_{R_e}) and ellipticity (ε) to distinguish between fast and slow rotators. Using the Pearson correlation coefficient between spatially resolved h_3 and V/σ within the isophotes of 2.5 half-light radii (R_e), we classified 1599 fast rotators into (i) 1073 galaxies showing a strong h_3 versus V/σ anticorrelation, indicative of normal rotating stellar discs as observed in earlier studies, and (ii) 526 galaxies exhibiting weak or no correlation between h_3 and V/σ. These galaxies are likely disturbed, showing signs of bars or merging. Further inspection revealed that 85 galaxies from the latter group contain an anticorrelated inner disc, with half of these inner discs composed of younger stellar populations, indicative of recent gas accretion and nuclear star formation. This catalogue presents measurements of high-order stellar kinematic moments, providing a basis for exploring their potential links with the kinematic structures of galaxies. We have made the newly extracted high-order kinematics publicly available for further studies on stellar dynamics and galaxy formation.

Key words: galaxies: evolution – galaxies: formation – galaxies: kinematics and dynamics – galaxies: stellar content.

1 INTRODUCTION

The line-of-sight velocity distribution (LOSVD) encodes key information about a galaxy's dynamics and assembly. In practice, the LOSVD is well described by a Gauss–Hermite expansion whose low-order moments provide the mean velocity (V) and velocity dispersion (σ), while the higher-order coefficients h_3 and h_4 quantify departures from a Gaussian (O. E. Gerhard 1993; R. P. der Marel & M. Franx 1993; R. Bender, R. P. Saglia & O. E. Gerhard 1994). The coefficient h_3 traces skewness and thus asymmetry in the LOSVD, whereas h_4 traces kurtosis and thus symmetric deviations. In non-rotating systems, flat-topped or peaked profiles are common, with $h_4 > 0$ typically associated with radial anisotropy and $h_4 < 0$ with tangential anisotropy (O. E. Gerhard 1993; R. P. der Marel & M. Franx 1993; O. Gerhard et al. 1998; J. Thomas et al. 2007). Recent work further suggests that h_4 carries information on star formation and lookback time in massive galaxies (F. D'Eugenio et al. 2023a, b).

A key discovery linking galaxy structure to kinematics emerged from the SAURON project, which kinematically separated early-type galaxies into *fast rotators* and *slow rotators* based on their projected specific angular momentum, λ_R (E. Emsellem et al. 2007). Fast rotators are typically flattened, disc-like systems with regular, large-scale rotation, while slow rotators are rounder, often triaxial systems with little net rotation. In a companion paper from that survey, M. Cappellari et al. (2007) used dynamical models to demonstrate that the λ_R kinematic classification is robust to inclination effects, showing that fast rotators are physically consistent with disc-like systems seen at various viewing angles, while slow rotators are physically quite different, weakly triaxial, systems. We adopt this standard kinematic classification terminology throughout the paper.

For rotation-supported discs, projection effects generate a well-known anticorrelation between V/σ and h_3 (e.g. R. P. der Marel & M. Franx 1993; D. Krajnović et al. 2006, 2011; D. R. Cole et al. 2014; Z. Wang et al. 2024). This trend is observed from early long-slit studies (e.g. R. Bender et al. 1994; R. P. Marel et al. 1994; A. Chung & M. Bureau 2004) to two-dimensional integral field unit (IFU) surveys such as SAURON (Spectroscopic Areal Unit for Research on Optical Nebulae; e.g. D. Krajnović et al. 2008; D. Krajnović et al. 2013), as well as in larger modern programmes like the SAMI (Sydney-Australian-Astronomical-Observatory Multi-object Integral-Field Spectrograph; e.g. J. de Sande et al. 2017) and in high-

★ E-mail: fuyq22@mails.tsinghua.edu.cn

quality MUSE (Multi-Unit Spectroscopic Explorer) data (e.g. S. I. Loubser et al. 2022; A. Fraser-McKelvie et al. 2025). Simulations reproduce the same behaviour and connect distinct patterns to specific formation channels: internal disc dynamics and bars generate the characteristic h_3 versus V/σ signature (e.g. M. Bureau & E. Athanassoula 2005; V. P. Debattista et al. 2005; R. Jesseit, T. Naab & A. Burkert 2005; M. Bois et al. 2011; F. Iannuzzi & E. Athanassoula 2015; A. Rantala et al. 2019; D. Zakharova et al. 2023), while gas-rich and gas-poor mergers imprint different loci at fixed V/σ (e.g. T. Naab, R. Jesseit & A. Burkert 2006a; T. Naab, S. Khochfar & A. Burkert 2006b; R. Jesseit et al. 2007).

T. Naab et al. (2014) used cosmological hydrodynamical zoom-in simulations of 44 individual central galaxies to link the high-order stellar kinematic features of these galaxies to their assembly history. Their Class A and B galaxies are fast rotators that experienced gas-rich mergers, and show a strong anticorrelation between h_3 and V/σ. Class D consists of fast rotators formed through gas-poor mergers, where h_3 and V/σ are not anticorrelated. Class C, E, and F are slow-rotating galaxies that either had late gas-rich mergers or gas-poor minor and/or major mergers. They find that fast rotators with a gas-rich merger history show the anticorrelation between h_3 and V/σ, whereas fast rotators with a gas-poor merger history do not.

J. de Sande et al. (2017) applied Gaussian mixture models to classify individual h_3 versus V/σ signatures of galaxies in the SAMI Galaxy Survey (J. J. Bryant et al. 2015) into five classes. From Class 1 to Class 5, galaxies gradually change from slowly rotating systems that exhibit no correlation between h_3 and V/σ (Class 1), to a strong anticorrelation in Class 3–4, and finally to fast rotating systems with a weak or nearly non-correlation in Class 5 (see Fig. 12 in J. de Sande et al. 2017). They find that weak or absent correlations often signal disturbed systems or the presence of counter-rotating bulges or bars, potentially exacerbated by limited spatial resolution.

Integral-field spectroscopy has enabled these advances by delivering spatially resolved kinematics for large samples. Surveys such as ATLAS^{3D} (M. Cappellari et al. 2011), CALIFA (S. F. Sánchez et al. 2012), and SAMI (J. J. Bryant et al. 2015) have transformed our view of galaxy formation and evolution (see reviews by M. Cappellari 2016; M. Cappellari 2026). The Sloan Digital Sky Survey IV (SDSS-IV) Mapping Nearby Galaxies at Apache Point Observatory (MaNGA) survey (K. Bundy et al. 2015) is the largest of these efforts, providing IFU spectroscopy for more than $\sim$ 10,000 galaxies. The official MaNGA Data Analysis Pipeline (K. B. Westfall et al. 2019) reports V and σ, but was not designed to deliver robust higher-order moments. Accurate measurement of h_3 and h_4 requires intrinsic dispersions that are at least a few times larger than the instrumental sampling (M. Cappellari & E. Emsellem 2004; M. Cappellari 2017), which for MaNGA is typically $\sigma_{\rm instr} \approx 70$ km s^{-1}. As a result, higher-order moments are unreliable for a substantial fraction of the sample, though they can be measured robustly for a well-defined subset. This motivates the present work.

In this paper we measure stellar kinematic parameters for MaNGA galaxies, with particular attention to the higher-order moments h_3 and h_4. We then identify and interpret the principal classes of h_3 and h_4 signatures in nearby galaxies and connect the observed moments to stellar population properties. These measurements will be used to constrain dynamical models in subsequent papers, and the resulting products will be released publicly.

This paper is organized as follows. In Section 2, we define a sample of slow and fast rotators with regular kinematic maps. In Section 3, we describe our extraction of high-order stellar kinematics. In Section 4, we present global properties of the high-order kinematics, introduce our classification for individual galaxies, and discuss the implications of this work.

2 DATA AND SAMPLE

This section shows the selection criteria for our sample galaxies from MaNGA survey.

2.1 The MaNGA Survey

The MaNGA survey (K. Bundy et al. 2015) is currently the largest IFU survey that provides a three-dimensional view of galaxies. The MaNGA data include a sample of 10 010 high-quality unique galaxy observations with spatially resolved spectra within the redshift range of $0.01 < z < 0.15$ (D. A. Wake et al. 2017). The spaxel size of MaNGA is 0.5 arcmin and the average full width at half-maximum (FWHM) g-band point spread function (PSF) throughout the survey is approximately 2.54 arcmin (D. R. Law et al. 2016).

The spectra provided by MaNGA cover a wavelength range of 3600 to 10 300 Å, with a spectral resolution $R \sim 2200$ (N. Drory et al. 2015; D. R. Law et al. 2016). Raw spectra are processed by the Data Reduction Pipeline (DRP) (D. R. Law et al. 2016), and products such as stellar kinematics and emission line properties are produced by the Data Analysis Pipline (DAP) (F. Belfiore et al. 2019; K. B. Westfall et al. 2019).

2.2 Sample Selection

In total, we have the DAP outputs of 10 010 high-quality unique galaxies and 135 repeat observations in SDSS DR17. For those with repeat observations, we have taken the better-quality observation.

The MaNGA spectrograph has a median spectral resolution of $\sigma_{\rm in} = 72$ km s^{-1} (D. R. Law et al. 2016) and the spectra are logarithmically rebinned with velocity steps $\Delta V = \sigma_{\rm in}$ by the DRP, to achieve a Nyquist sampling of the data. D. R. Law et al. (2021) concluded that it is possible to recover velocity and dispersion well below the instrumental resolution. However, the same is not true for the h_3 and h_4. Fig. 9 in M. Cappellari (2017) illustrates the PPXF recovery of the kinematics, when the astrophysical velocity dispersion $\sigma \lesssim 2\Delta V$, it becomes difficult to constrain the Gauss-Hermite moments due to undersampling (M. Cappellari & E. Emsellem 2004; M. Cappellari 2017). For MaNGA, $2\Delta V \approx 140$ km s^{-1}. To avoid undersampling, we used the flux-weighted mean stellar velocity dispersion.[1] $\langle\sigma\rangle_{\rm e}$ of all spaxels within one effective radius ($1R_{\rm e}$) provided by the DAP and restricted our sample to MaNGA galaxies with $\langle\sigma\rangle_{\rm e} \gtrsim 140$ km s^{-1}. This yields 2583 galaxies.

We then remove galaxies with low data quality (Qual $= -1$) according to the kinematic quality flags in K. Zhu et al. (2023), which provides a visual quality classification of stellar kinematics. The quality flags used here are based on visual inspection of the recovered $V_{\rm rms}$ and V maps with the MFL (mass follow light) model, taken from the catalogue of K. Zhu et al. (2023, section 5.1) under the keyword `'Qual'`. Qual $= -1$ means these galaxies are of very

[1]We want to use $\langle\sigma\rangle$ here, not the $V_{\rm rms} \equiv \sqrt{V^2+\sigma^2}$, which is commonly used to study galaxy properties, because the undersampling is affected by the broadening of the lines, but not by the resolved rotation.

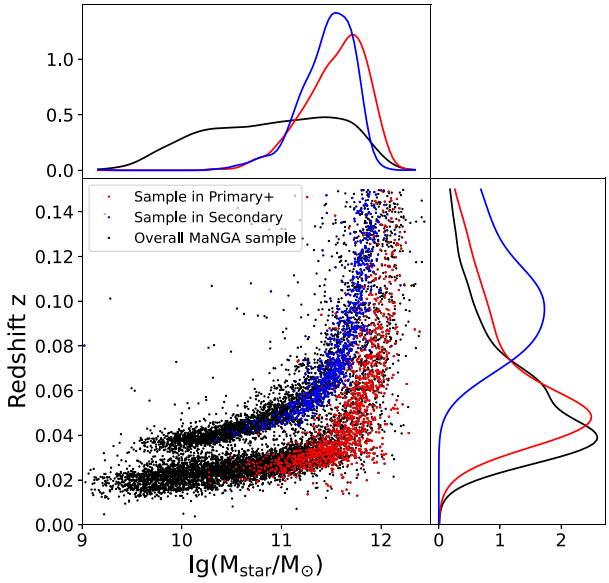

Figure 1. Distribution of our galaxy sample in comparison to the full MaNGA sample in the stellar mass–redshift plane. Black lines and dots represent all galaxies from the MaNGA survey, while red and blue ones correspond to galaxies in our sample belonging to the primary+ and secondary subsamples, respectively.

low quality. We should not trust any of the kinematic properties of these galaxies. After removing all the Qual $= -1$ galaxies from our sample, there are 2230 galaxies left.

The full MaNGA sample consists of three main subsamples. The combination of primary and colour-enhanced samples is called the primary+ sample, which makes up 67 per cent of the targets, is designed to be covered by the IFUs to $1.5R_e$. The Secondary sample, which makes up the rest 33 per cent, is designed to cover $2.5R_e$ (D. A. Wake et al. 2017). Fig. 1 compares the sample used in this work with the overall MaNGA sample. Our sample consists of 1341 galaxies (∼60 per cent) from the primary+ sample and 889 galaxies (∼40 per cent) from the Secondary sample, showing a modest 7 per cent bias toward the Secondary sample. Our sample is significantly biased toward the high-mass end compared to the overall MaNGA sample. This is an expected consequence of selecting galaxies with a high central velocity dispersion, as the galaxies are in virial equilibrium (e.g. J. Binney & G. A. Mamon 1982).

3 METHODS

In this section, we show how we derive four kinematic moments (V, σ, h_3, h_4) with the help of the PPXF software (M. Cappellari & E. Emsellem 2004; M. Cappellari 2017, 2023). In Section 3.1, we shall first briefly introduce PPXF. In Section 3.2, we describe how we construct stellar templates based on the MaStar stellar library. In Section 3.3, we discuss how we determine the level of bias when running PPXF. In Section 3.4, we estimate the systematic errors introduced during the model-fitting process.

3.1 The PPXF software

Our stellar kinematic fitting is based on the version 8.2[2] of PPXF. This penalized pixel-fitting software (PPXF) pioneered a robust pixel-fitting method, particularly optimized for extracting the kinematics of the stars and gas in galaxies from integral field spectroscopic (IFS) data.

When fitting the stellar kinematics, an additive Legendre polynomial is used to correct for possible mismatches between the stellar continuum emission from the observed galaxy spectrum and the template due to small errors in the flux calibration and minor template mismatch effects. We applied an 8th-order additive Legendre polynomial to remove residuals.

3.2 Optimal subset of templates from the Mastar Library

In DR17, stellar kinematics measurements are based on the MILES-HC library (Abdurro'uf et al. 2022). Since MILES (A. Vazdekis et al. 2010, 2015) only spans between 3575 and 7400 Å, this means that stellar kinematics does not include, for example, contributions from the calcium NIR triplet near 8600 Å. The MaStar stellar library (R. Yan et al. 2019; Abdurro'uf et al. 2022) allows us to take advantage of the full MaNGA spectral range (3600 to 10 000 Å).

To reduce computation time when using large stellar libraries as templates, we applied the hierarchical clustering method and software[3] described in K. B. Westfall et al. (2019, Section 5) to select subsamples of stars that are representative of the entire library.

The spectral resolution of the spectra in the MaStar library varies with wavelength. The resolution curve also differs from star to star and from visit to visit. In order to provide subsets of spectra that have been unified in their resolution curves, we adopt the 60th percentile resolution curve in Abdurro'uf et al. (2022, section 6.3). For this resolution curve, Abdurro'uf et al. (2022) has selected visit spectra that have sharper line spread-functions (LSFs) (higher resolution) than it at all wavelengths. We use equation (5) from M. Cappellari (2017) to homogenize the resolution of all stars in the library to the same σ_{inst} of the adopted 60th percentile resolution curve, while accounting for the variable instrumental dispersion σ_{temp} of each selected visit spectra. We broaden the visit spectra to the 60th percentile resolution curve using the procedure VARSMOOTH within the PPXF package, which allows for a variable convolution kernel. As an upgrade of what has been done in Abdurro'uf et al. (2022), this new function uses the fast Fourier transform and the analytic Fourier transform of a Gaussian to avoid under-sampling issues (M. Cappellari 2023, algorithm 1).

After convolving every selected visit spectra to uniform resolution, the multiple visit spectra for each star are combined into one spectrum per star. The key idea of the hierarchical clustering method is to apply a clustering algorithm (A. K. Jain, M. N. Murty & P. J. Flynn 1999) to the N spectral templates composed of M spectral channels by treating them as N vectors in an M-dimensional space (K. B. Westfall et al. 2019, section 5). The distance between two spectra is calculated as one-half of the interval enclosing 95.45 per cent (2σ confidence) of the residuals, in a PPXF fit of one spectrum using another spectrum as the template. The distances are used to construct a distance matrix for input to a hierarchical clustering algorithm. To avoid a large

[2]Python PPXF package v8.2 from https://pypi.org/project/ppxf/.
[3]We used the procedure SPECLUS available on https://github.com/micappe/speclus

systematic error at the blue and red end of the star spectrum, we used 3680–9900 Å instead of the full wavelength coverage of the MaStar spectrum when fitting. For this exercise, we include an eighth-order additive Legendre polynomial in the PPXF fits to be consistent with the method used when fitting the stellar kinematics of the galaxy spectra.

The SPECLUS procedure generated 56 clusters (i.e. groups of stars) out of 5090 high-resolution stars. We normalize all stars for every cluster and take the average. We remove two templates with prominent emission lines, resulting in a final set of 54 spectra in our template library, as shown in Fig. 2. Although the clustering of the stellar templates does not use any information on their stellar population parameters, as one would expect, the clusters tend to concentrate in regions of similar population parameters, as shown in Fig. 3.

The MaNGA DAP constructed similar MASTARHC2 templates (Abdurro'uf et al. 2022) to model the galaxy continuum for emission line measurements in DR17. Our new templates are constructed including additive polynomial in the fit, consistent with what we used when fitting the stellar kinematics of the galaxy spectra. Moreover, in our approach we homogenize the stellar spectra to the same resolution using new VARSMOOTH procedure to avoid undersampling (see section 3.1 in M. Cappellari 2023). Our stellar templates are available online[4]

3.3 Kinematic extraction including h_3 and h_4

Before extracting the kinematic it is important to spatially bin the data to increase the S/N. This is to reduce possible biases to the kinematics which can happen when the fitted solution is allowed to strongly deviate from the true one, due to the too low S/N. For this reason, we Voronoi binned[5] (M. Cappellari & Y. Copin 2003) the IFU spectra to $S/N = 30$ before the kinematic extraction. Unlike what was done in the DAP pipeline, we ignore the spatial correlation between spaxels. This is to reduce the loss of spatial resolution at large radii and low S/N, at the expense of a slightly smaller S/N than the target value.

To extract the Gauss-Hermite moments with PPXF it is recommended to penalize the kinematics to reduce the noise. This requires determining the penalty parameter (`bias` keyword in PPXF), which depends on the S/N of the spectrum and fitted wavelength range (M. Cappellari & E. Emsellem 2004). Now we determine the level of bias. As discussed in detail in M. Cappellari & E. Emsellem (2004) and M. Cappellari et al. (2011), we adjusted the penalty in PPXF through Monte Carlo simulation in Fig. 4. Following the PPXF documentation, we ensure for the extracted values not to deviate significantly from the true values at the adopted $S/N = 30$ and for $\sigma_{\rm in} > 2\Delta V$. The recovered values can only deviate at smaller $\sigma_{\rm in}$, where the data do not contain enough information to recover the full LOSVD. The resulting adopted level is `bias` $= 0.3$.

When running PPXF, we remove emission lines by masking around the following lines [O II], H δ, H γ, H β, [O III], [O I], H α, [N II], and [S II]. The outliers in the spectrum are removed using the `'fit-and-clean'` method, which means that we run PPXF twice on each binned spectrum. The first fit includes only the masks for the emission lines. After the first fit, we perform a 3σ outlier clipping

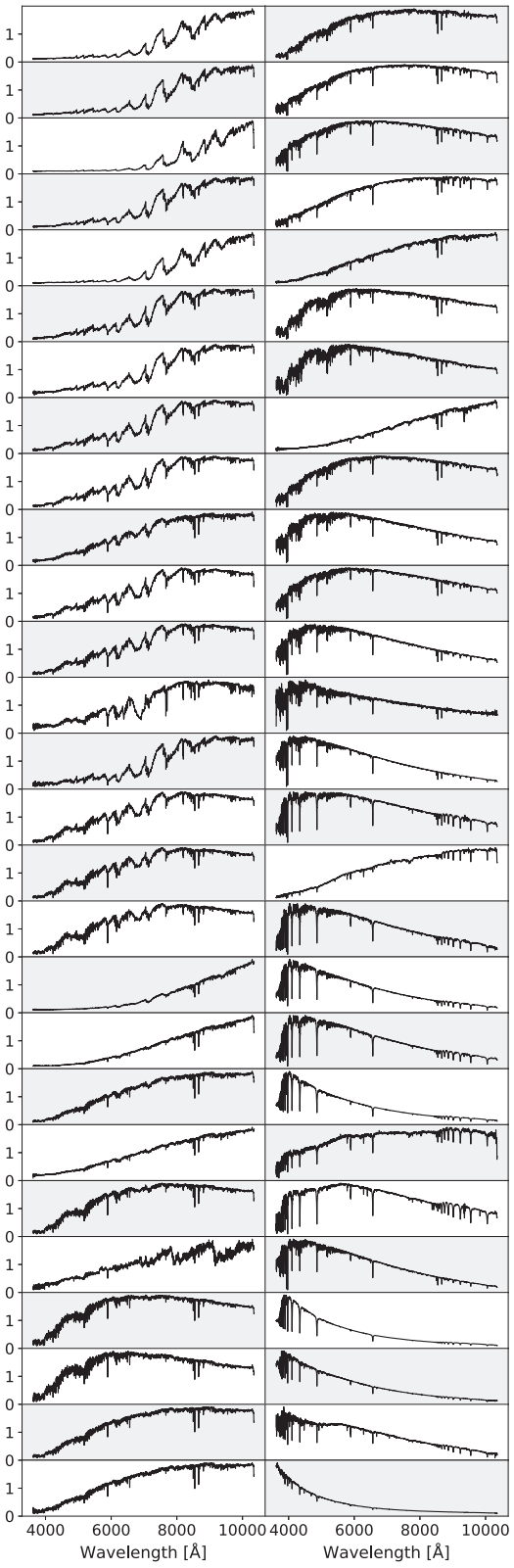

Figure 2. The 54 templates in the template library. The spectra are ordered from cold to hot according to median temperature of their cluster. Note that some hot spectra appear red due to reddening. The spectra are normalized by their median value.

[4]Available from https://github.com/Fuyq42/MaNGA_High_Order_stellar_kinematic, see Mastar_hierarchical_clusters.fits.
[5]We used v3.1 of the VORBIN package from https://pypi.org/project/vorbin/.

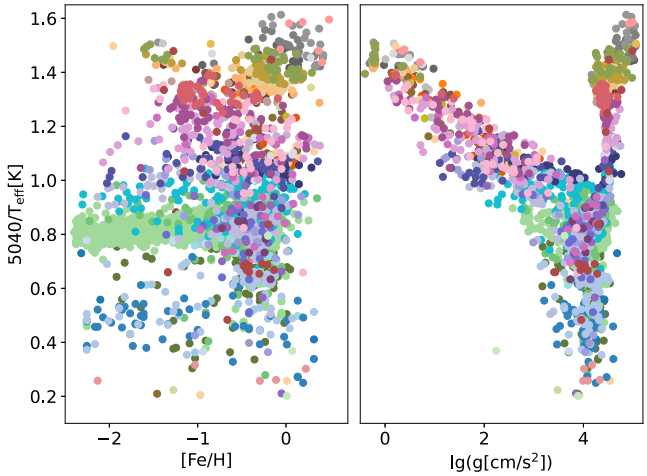

Figure 3. Effective temperature ($T_{\rm eff}$), metallicity, and log surface gravity g of the stars in the MaStar stellar library. Each datum is assigned a colour based on its assigned cluster from the hierarchical-clustering algorithm. The population parameters come from L. Hill et al. (2022).

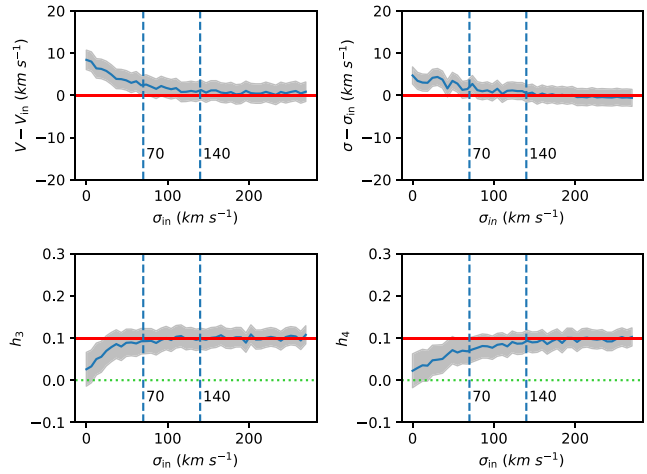

Figure 4. Testing penalization in PPXF. We simulated spectra with the S/N= 30 of our data and an LOSVD with h_3 =0.1, h_4 =0.1 and σ in the range between 30 and 300 km s^{-1}. We extracted the kinematics with PPXF and a penalty bias = 0.3. The solid blue lines in the top two panels show the median of the differences between the measured values and the input values of the mean velocity and the velocity dispersion. The shaded area represent the 16th and 84th percentiles of the same differences (1σ). The bottom panels show the same lines for the recovered values of h_3 and h_4. The blue dashed lines are reference lines of one and two times the MaNGA spectrum resolution. Compared with the input values (0.1, red line), The h_3 and h_4 parameters can only be recovered without bias when $\sigma_{\rm in} \geq$ 140 km s^{-1}.

based on the residual between the best-fitting template and the observed galaxy spectrum and add clipped pixels to the original masked emission line regions and repeat the fit. Removing emission lines and outliers ensures a nearly smooth residual across the entire spectrum.

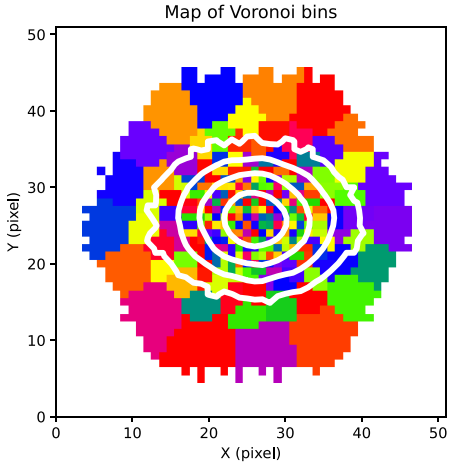

Figure 5. The Voronoi bins of our example galaxy (MaNGA-ID: 1–149878). The contour lines indicate the surface brightness of the example galaxy.

3.4 Negligible effect of spatial binning on h_3 and h_4

The process of co-adding multiple spectra, such as through seeing effects (PSF convolution) or Voronoi binning, can artificially generate non-zero higher-order kinematic moments (h_3 and h_4). This occurs because summing spectra with different line-of-sight velocities produces a combined line profile that is no longer perfectly Gaussian, even if each individual spectrum was. To ensure our results are robust, we performed a simulation to precisely quantify the magnitude of this systematic effect and demonstrate that it is negligible for our analysis.

Our simulation strategy involves three steps:

(i) Create an idealized mock datacube where the kinematics are perfectly Gaussian everywhere.

(ii) Degrade this cube by simulating our exact observational and binning procedure.

(iii) Measure the resulting kinematics to isolate the systematic error.

First, we constructed the 'ground truth' model. We selected a representative galaxy (MaNGA-ID: 1–149878) with regular kinematics and used the JAMPY package[6] (M. Cappellari 2008, 2020) to generate smooth, noise-free 50 × 50 spaxel maps, sampled at 0.″5 per spaxel, of the velocity (V) and velocity dispersion (σ). For the models, we adopted a cylindrically aligned velocity ellipsoid and used the mass-follows-light models with the corresponding best-fitting parameters from K. Zhu et al. (2023). We then used these maps to build a mock datacube. At each spaxel, a single stellar template was convolved with a perfect Gaussian LOSVD defined by the local V and σ. The flux in each spaxel was scaled according to a Multi-Gaussian Expansion model derived from the galaxy's SDSS r-band image (see Section 3.2 in K. Zhu et al. 2023). By design, this mock datacube has a perfectly Gaussian LOSVD at every single spaxel. *Therefore, in this idealized model, the true intrinsic values are* $h_3 = 0$ *and* $h_4 = 0$ *everywhere* before any spatial mixing.

Next, we simulated our measurement process. Each wavelength slice of the mock cube was convolved with the MaNGA PSF (FWHM

[6]Python v8.0 from https://pypi.org/project/jampy/.

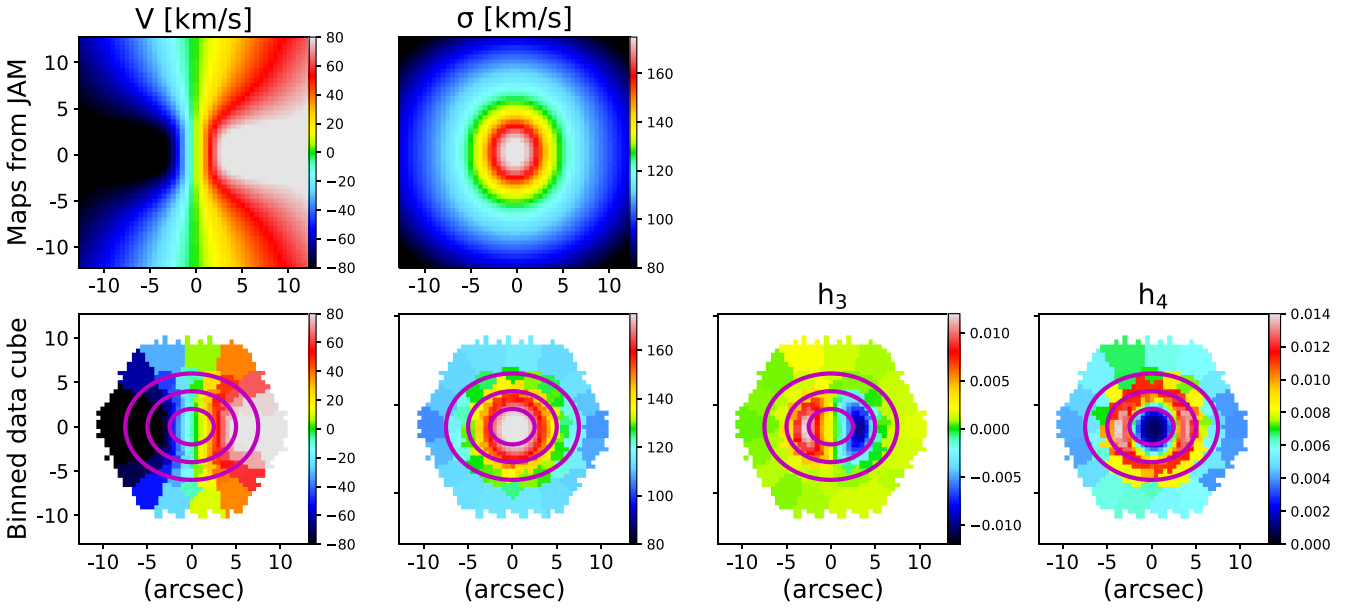

Figure 6. The simulation of systematic errors induced by the PSF and spatial binning. The columns correspond to the four moments of the LOSVD. The first row shows the velocity and dispersion maps generated from JAM, which are assumed to be noiseless and do not include h_3 and h_4. The second row presents the fitting results from the convolved datacube after Voronoi binning. Any non-zero h_3 and h_4 measured at this stage are, by definition, purely systematic artefacts. Magenta contour lines indicate the surface brightness distribution of the example galaxy. The maps are colour-coded by V, σ, h_3, and h_4, respectively. The tick labels on the spatial axes are in units of arcseconds.

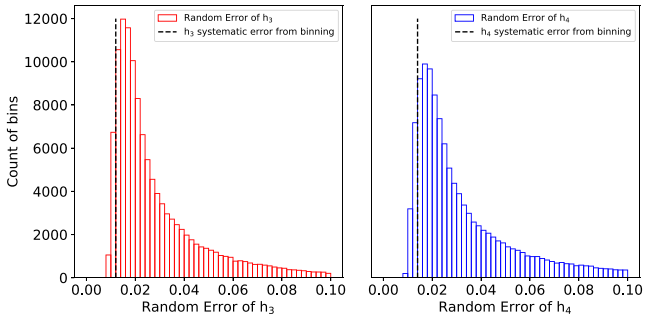

Figure 7. These two histograms compare the random and systematic errors from binning of h_3 and h_4. The random errors are the output formal error of each bin by `pPXF`, while the black dashed lines indicate the systematic errors from binning. For h_3, the systematic error is 0.012; for h_4, it is 0.014.

$= 2''.54$). Afterwards, we binned the spaxels in this convolved cube using the exact Voronoi binning scheme from the real observations of the galaxy (see Fig. 5).

Finally, we fitted the spectrum of each *bin* with `pPXF` to measure the kinematics, as shown in the bottom row of Fig. 6. *Any non-zero h_3 and h_4 measured at this stage are, by definition, purely systematic artefacts*, as they were generated entirely by the process of PSF convolution and Voronoi binning acting on a model that was constructed to have $h_3 = 0$ and $h_4 = 0$ at every location.

The results of this simulation provide a robust upper limit on the systematic errors. The maximum absolute values introduced are approximately 0.012 for h_3 and 0.014 for h_4. As shown in Fig. 7, this systematic error is significantly smaller than the random errors from our actual measurements. The median measured absolute values of h_3 and h_4 in our galaxy sample are 0.11, with median random errors of $\Delta h_3 = 0.023$ and $\Delta h_4 = 0.025$. Indeed, 94 per cent of the random errors in h_3 and 91 per cent of those in h_4 are larger than these systematic effects. We can therefore safely conclude that, although the biases are not entirely negligible, our scientific results are not significantly impacted by systematics introduced by spatial binning and seeing.

4 RESULTS

In this section, we present the results of our kinematics extraction (Section 3) of h_3 and h_4 for the sample of 2230 galaxies as described in Section 2.2 and present some global properties. A comparison between 4-moments LOSVD present in this paper and the best-fitting Gaussian moments in DAP (K. B. Westfall et al. 2019) is shown in Appendix A. The kinematic maps will be available online[7] The format of data are presented in Appendix B.

We will study the qualitative appearance of the galaxy velocity moments based on 2D kinematic. In Section 4.3, we try to identify high-order kinematic signatures that occur more frequently than others and sort them into separate classes. Section 4.4 presents the integrated galaxy properties of these classes. In Section 4.5, we discuss the impact of galaxy bars and mergers in higher-order terms by comparing observations with simulations.

4.1 Separating fast and slow rotators

Following E. Emsellem et al. (2007, 2011), we use the spin parameter ($\lambda_{\rm Re}$) to separate fast-rotating galaxies from slow-rotating galaxies.

[7]Available from https://github.com/Fuyq42/MaNGA_High_Order_stellar_kinematic. The total size of the kinematic files for our galaxies is about 900 MB.

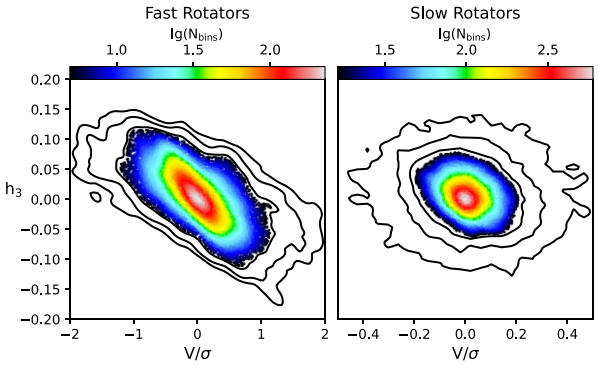

Figure 8. Local h_3– V/σ relation for all bins of fast rotators (left) and slow rotators (right). The panels are colour-coded by the number density of bins. In low number density regions at the periphery of each panel, the number density is displayed by contour lines. These bins with larger velocities and h_3 are mainly located in regions with lower SNR at the outer part of a galaxy.

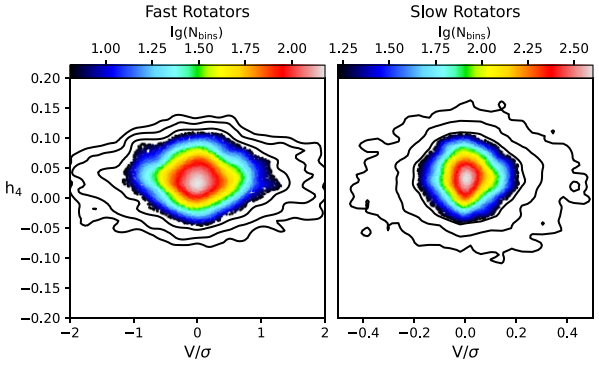

Figure 9. Local h_4– V/σ relation for all bins of fast rotators (left) and slow rotators (right). The panels are colour-coded as in Fig. 8.

$\lambda_{\rm Re}$ is derived from the following definition (E. Emsellem et al. 2007):

$$\lambda_{R_e} = \frac{\sum_k F_k R_k |V_k|}{\sum_k F_k R_k \sqrt{V_k^2 + \sigma_k^2}}, \quad (1)$$

where F_k, V_k, and σ_k are the flux, stellar velocity, and stellar velocity dispersion in the kth IFU spaxel. R_k is the distance of k-th spaxel to the galaxy centre. The summation is defined within the elliptical half-light isophote. We use the λ_{R_e} measurement in K. Zhu et al. (2024), where the beam smearing effect has been corrected following M. T. Graham et al. (2018).[8] The λ_{R_e} values are not inclination-corrected. We define the slow rotators (SRs) as the galaxies satisfying $\lambda_{R_e} < 0.08 + \varepsilon/4$ and $\varepsilon < 0.4$ (where ε is the observed ellipticity within the half-light isophote, see the shaded region in Fig. 16) following M. Cappellari (2016, equation 19), while the fast rotators (FRs) are defined to be the galaxies outside the region occupied by the slow rotators. Under this definition, the galaxies used in this paper consist of 631 slow rotators and 1599 fast rotators. Compared with the distribution of fast and slow rotators in the overall MaNGA sample shown in Fig. 8 of K. Zhu et al. (2023), our sample exhibits a strong bias toward slow rotators. This selection bias is expected, as MaNGA slow rotators are typically more massive and possess higher velocity dispersions (M. T. Graham et al. 2018; K. Zhu et al. 2023, 2024).

[8] https://github.com/marktgraham/lambdaR_e_calc

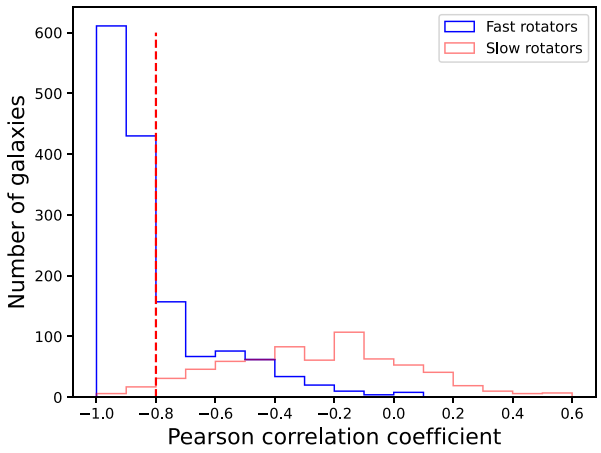

Figure 10. The distribution of the Pearson correlation coefficient in our sample of 2230 galaxies. Fast rotators are coloured in blue and slow rotators are coloured in red. We are using the Pearson correlation coefficient −0.8 (dashed red line) as the dividing line to classify fast rotators into two categories.

4.2 Correlations of h_3 and h_4 with V/σ

In Fig. 8, we plot the local h_3– V/σ relation for all data points in our galaxies. There are distinct differences between the distribution of fast and slow rotators. We confirm the classical anticorrelation (e.g. R. Bender et al. 1994; D. Krajnović et al. 2008; J. de Sande et al. 2017) of h_3 and V/σ in fast rotators. The slow rotators have smaller V/σ values by definition and generally small amplitudes of h_3. There is no clear correlation between h_3 and V/σ in slow rotators. This makes sense since slow rotators have no discs and are instead dominated by random motion rather than rotation.

In Fig. 9 we plot the local h_4– V/σ relation for all data points in our galaxies. The distribution of h_4 for fast and slow rotators is mildly positive on average. The positive h_4 is consistent with Fig. 3(b) in J. de Sande et al. (2017) where they find the median h_4 in the SAMI data is 0.05. Unlike h_3, there is no significant difference in the range of values for h_4 between fast rotators and slow rotators. The median h_4 is slightly lower in fast rotators (0.03) compared to slow rotators (0.05). This difference may arise because a large fraction of fast rotators exhibit relatively low h_4 values near their centres. This feature is further illustrated in Section 4.3.

4.3 Galaxy kinematic classification with h_3 and h_4

Simulations provide us with three distinct patterns in h_3 versus V/σ (T. Naab et al. 2014, Fig. 9). Following the high-order patterns as presented in T. Naab et al. (2014) and the similar classification by J. de Sande et al. (2017), we explore the classification of individual galaxies for MaNGA data using their h_3– V/σ diagram and the distance of bins to the galaxy centre (in units of R_e). We do this by calculating the Pearson correlation coefficient between h_3 and V/σ within $0.5R_e$ and $2.5R_e$ isophotes for our galaxies.

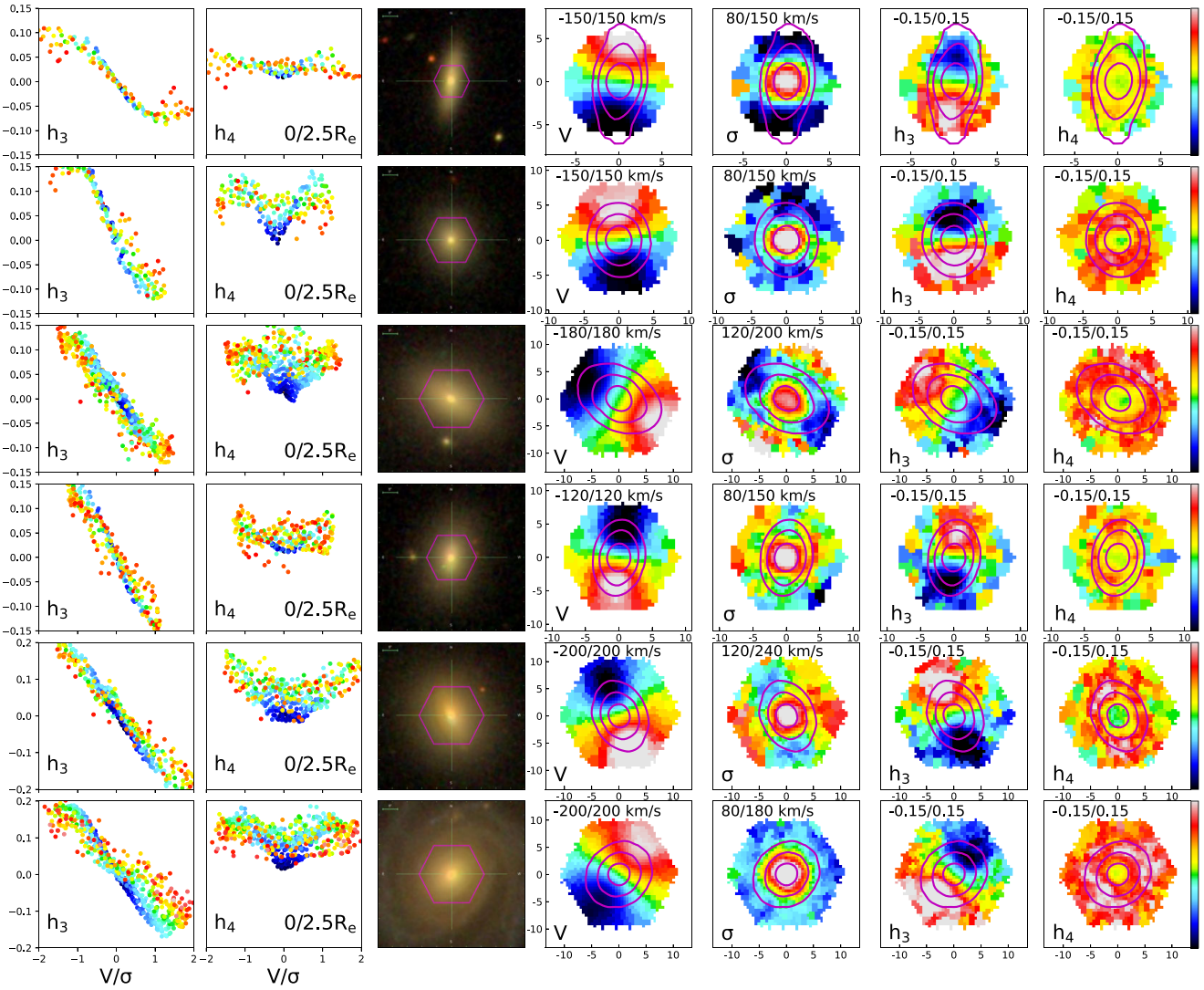

Figure 11. Examples of six Class A fast rotators with anticorrelated $h_3 - V/\sigma$ relation (MaNGA-ID: 1–44536, 1–137799, 1–217050, 1–277161, 1–613211, 1–269085 from top to bottom). For each galaxy, the two left panels are local values within 2.5R_e of h_3 and h_4 versus V/σ, coloured by the mean distance from the centre in units of R_e. The range for the colourbar is shown in the bottom right. From the third one from the left, we show the galaxy images from MaNGA and two-dimensional stellar kinematics maps for these galaxies. The range for the colourbar is written in the upper left. The solid magenta contour lines represent the surface brightness. The tick labels on the spatial axes of rows 4–7 are in units of arcseconds.

For galaxies in the primary+ sample whose field of view does not extend to 2.5R_e, all available Voronoi bins are included in our analysis. The inclusion of these outermost bins makes our results depend mildly on whether we ignore the covariance in the Voronoi binning process. The Voronoi binning method provides a general framework for computing the signal-to-noise ratio (S/N) of a bin resulting from the co-addition of multiple spaxels. A common approach, and the one we adopt, is to co-add the noise from individual spaxels in quadrature, which assumes the noise between spaxels is uncorrelated. An alternative is to account for the spatial covariance between spaxels, which results in a slower S/N increase as spaxels are co-added. We choose to ignore covariance to favour a higher spatial resolution. As demonstrated in fig. 9 of K. B. Westfall et al. (2019), for a given target S/N, this choice leads to a larger number of bins in the outer regions of galaxies. Since these outer regions are typically disc-dominated and exhibit a strong h_3– V/σ anticorrelation (e.g. D. Krajnović et al. 2011), our method populates the anticorrelation in Fig. 8 with more data points. While this may alter the density contours, it does not change the fundamental shape of the observed relation.

The distribution of the Pearson correlation coefficient within 2.5R_e is shown in Fig. 10. It can be seen from the histogram that there is a significant difference between fast and slow rotators. As a quantitative measure of the trend shown in Fig. 8, the fast rotators show a clear anticorrelation between h_3 and V/σ while there are no correlation in most slow rotators.

After manually inspecting kinematic maps with different Pearson correlation coefficients, we find that the Pearson correlation coefficient -0.8 can be used as the dividing line to classify fast rotators into two categories. 1073 fast rotating galaxies with Pearson correlation coefficient smaller than -0.8 are normal fast rotators with anticorrelated h_3– V/σ. These galaxies account for two-thirds of the

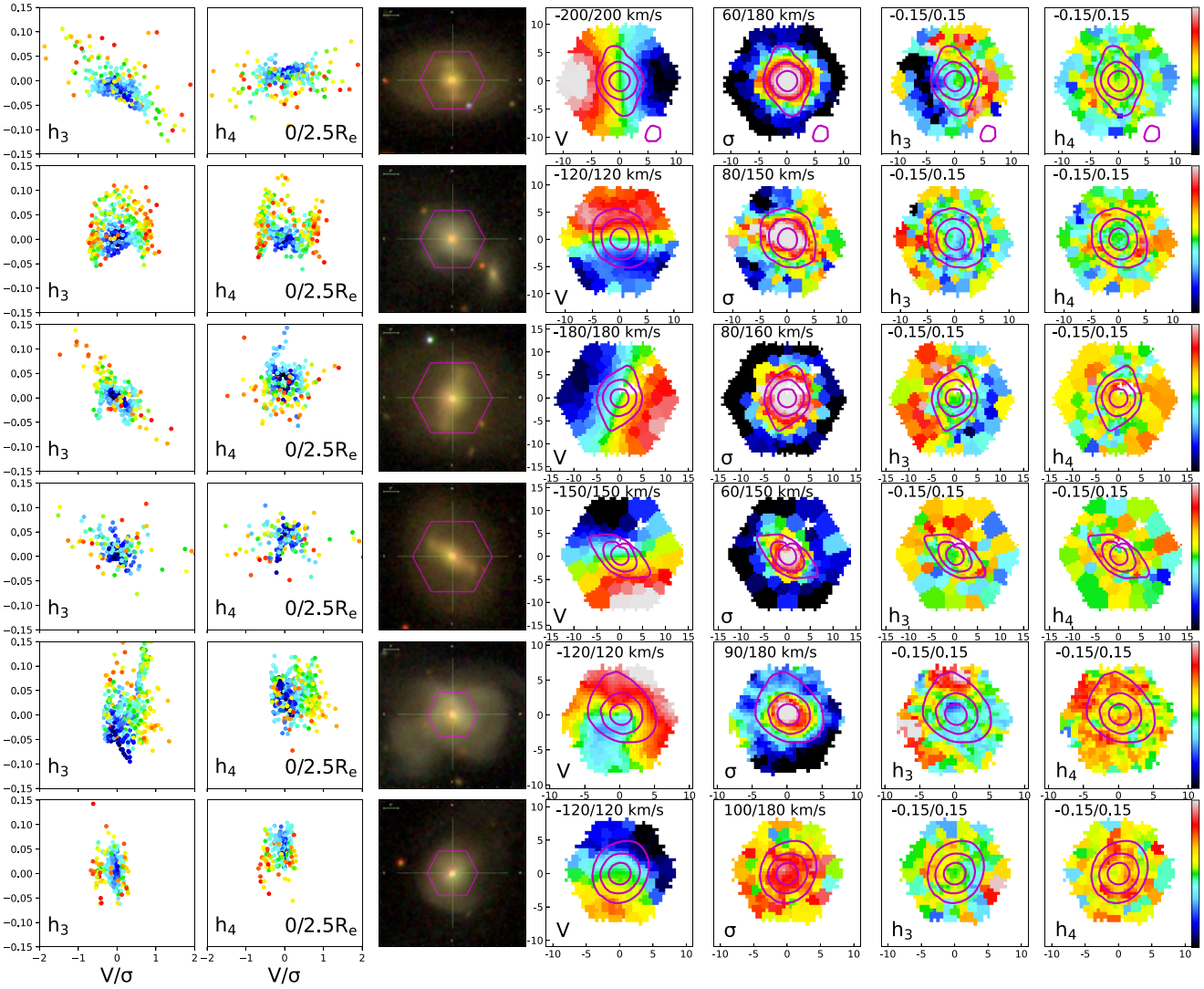

Figure 12. Examples of six Class B fast rotators with non-correlated $h_3 - V/\sigma$ relation (MaNGA-ID: 1–378148, 1–585632, 1–594505, 1–378881, 1–631278, 1–560826 from top to bottom). The symbols are the same as in Fig. 11.

Table 1. Example catalogue of Pearson coefficient within 2.5R_e and 0.5R_e isophote for 5 fast rotators in our sample. A machine-readable version of the full table is available as supplementary material on the journal website.

MaNGA-ID	Pearson coefficient (2.5R_e)	Inner Pearson coefficient (0.5R_e)	Class	Target Flag
1–382273	−0.933	−0.962	Anticorrelated	0
1–547191	−0.877	−0.921	Anticorrelated	2
1–378148	−0.542	−0.688	Non-correlated	0
1–585632	−0.275	−0.401	Non-correlated	0
1–605551	−0.626	−0.962	Inner Anticorrelated	0

Note. Column (1) is the MaNGA identification ID. Column (2–3) are Pearson coefficients between h_3 and V/σ within 2.5R_e and 0.5R_e isophote. Column (4) gives the classification results. Column (5) is the target flag for subsample of MaNGA (primary: 0, secondary: 1, colour enhanced: 2)

1599 fast rotators, corresponding to model Classes A and B in T. Naab et al. (2014) and Class 3–4 in J. de Sande et al. (2017). There are no galaxies with a Pearson coefficient greater than +0.8, indicating that no galaxies in our sample show a positive correlation between h_3 and V/σ with equal credibility. 526 fast rotating galaxies with Pearson correlation coefficient larger than −0.8 are classified as fast rotators with non-correlated h_3 and V/σ. This global classification does not account for the presence of multiple kinematic components or strong

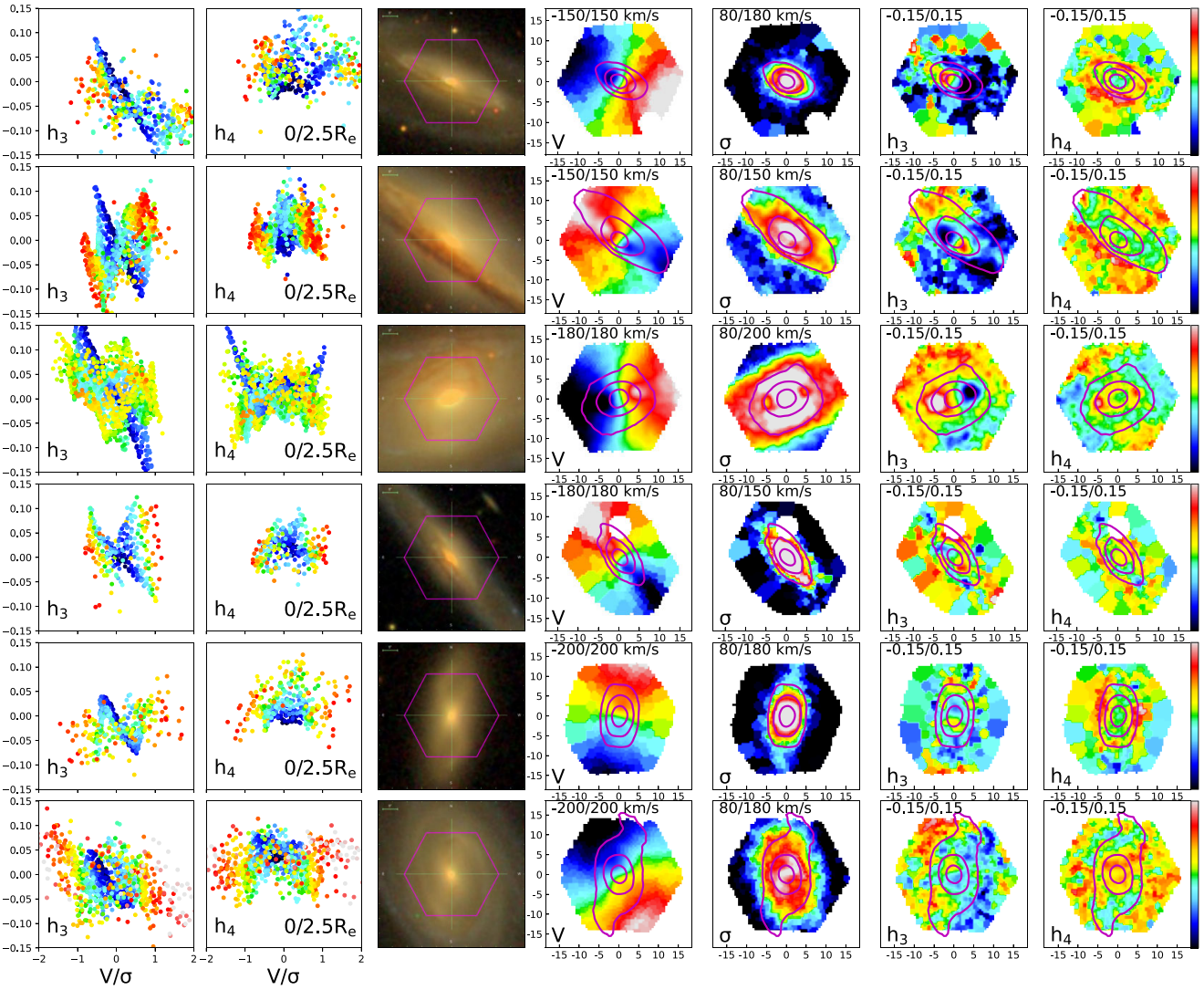

Figure 13. Examples of six Class C fast rotators with inner-correlated $h_3 - V/\sigma$ relation (MaNGA-ID: 1–38101, 1–90190, 1–605551, 1–605195, 1–54539, 1–457427 from top to bottom). The symbols are the same as in Fig. 11.

merger signatures, which can blend correlations and anticorrelations, resulting in a Pearson correlation coefficient near zero. Galaxies with multiple kinematic structures may be classified as non-correlated. Slow rotators are not further classified based on this h_3– V/σ diagram within 2.5R_e isophotes.

Fig. 11 shows examples of fast rotators with anticorrelation, which account for two-thirds of fast rotators. This is consistent with the results of simulations and previous observations of rotating discs (e.g. R. Bender et al. 1994; T. Naab et al. 2006a; R. Jesseit et al. 2007; D. Krajnović et al. 2008; J. de Sande et al. 2017). A large fraction of galaxies in this class also shows low h_4 values around the centre, corresponding to Class A galaxies in T. Naab et al. (2014) that display a V-shaped structure in the h_4–V/σ diagram. J. de Sande et al. (2017) also finds a heart-shaped pattern in h_4 versus V/σ diagram for regular rotators (J. de Sande et al. 2017, see their fig. 9).

Fig. 12 shows the kinematic maps of non-correlated fast rotators. We found that this type of galaxy can still be divided into two subclasses: the majority, consisting of 441 galaxies, shows steep and insignificant correlation, while the rest (85 galaxies) have inner anticorrelations. The first subclass corresponds to model Class D in T. Naab et al. (2014). The simulation reveals that these galaxies have recently undergone gas-poor major merger. However, manual inspection revealed that many of these galaxies exhibit features of merging or bars morphologically. We will discuss the influence of galaxy bars and mergers on h_3 in Section 4.5. Examples for the second subclass (85 galaxies) are shown in Fig. 13. For these galaxies, even though the Pearson coefficient calculated within 2.5R_e isophote is larger than -0.8, we can still observe a h_3 disc near the centres (usually within 0.5R_e) of these galaxies, showing an distinct anticorrelation between h_3 and V/σ. Table 1 includes the Pearson coefficient within 2.5R_e and 0.5R_e isophote for fast rotators. A machine-readable version of the table is available as supplementary material on the journal website. 1599 fast rotators are classified into three categories: anticorrelated, non-correlated, and inner anticorrelated galaxies. Similar to fig. 9 in T. Naab et al. (2014), we present the local relation between V/σ and h_3 as well as h_4 of all data points within one effective radius for all example galaxies of every class in Fig. 14 (example galaxies are shown in

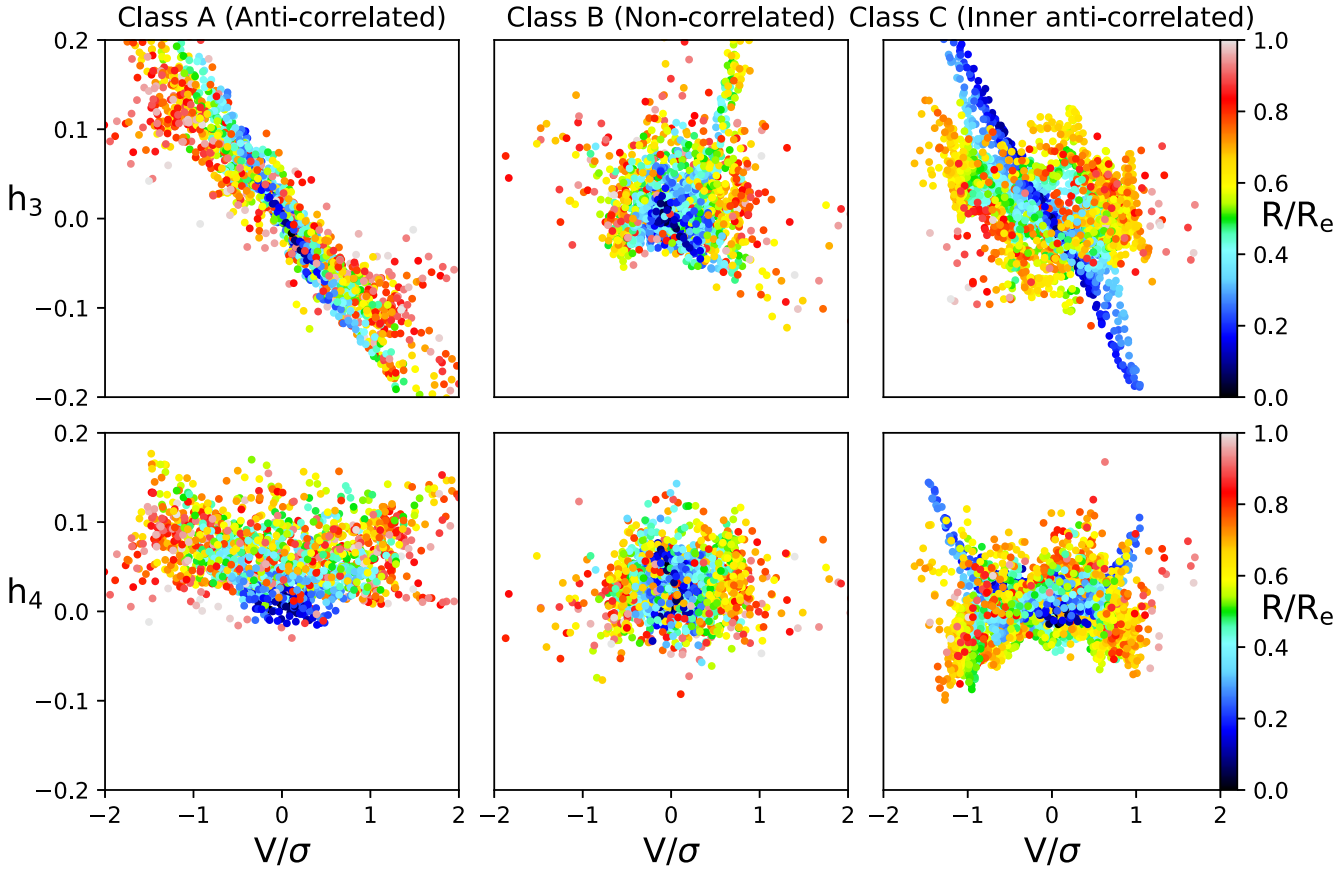

Figure 14. Local values of h_3 and h_4 versus V/σ diagrams for all example galaxies in the three kinematic classes, coloured by the mean distance from the centre in units of R_e. Anticorrelated FRs are fast rotators with anticorrelated h_3 and V/σ (the Pearson correlation coefficient smaller than -0.8 within $2.5R_e$). Non-correlated FRs are galaxies with Pearson correlation coefficient larger than -0.8 within both $2.5R_e$ and $0.5R_e$ isophote. Inner anticorrelated FRs are galaxies where Pearson correlation coefficient are larger than -0.8 within $2.5R_e$ but smaller within $0.5R_e$ isophote.

Figs 11–13, six per class). We provide the detailed definitions of the three types of galaxies below, referring to them as Class A, B, and C. The flowchart in Fig. 15 provides a clearer and more intuitive illustration of how we arrive at this classification step by step.

(i) **Anticorrelated fast rotators (Class A)**: Fast rotators with a Pearson correlation coefficient $r(2.5R_e) < -0.8$.

(ii) **Non-correlated fast rotators (Class B)**: Fast rotators with $r(2.5R_e) > -0.8$ and $r(0.5R_e) > -0.8$.

(iii) **Inner anticorrelated fast rotators (Class C)**: Fast rotators with $r(2.5R_e) > -0.8$ but $r(0.5R_e) < -0.8$.

4.4 Galaxy properties of high-order stellar kinematic classes

In the previous section, the fast rotators were separated into three classes based on their $h_3 - V/\sigma$ diagrams within $2.5R_e$ isophotes. Here, we will look at the integrated galaxy properties of these classes.

The distribution of galaxies in the $(\lambda_{R_e}, \varepsilon)$ plane is shown in Fig. 16. The definition of λ_{R_e} and ε are mentioned in Section 4.1. Non-correlated galaxies rotate more slowly. The majority of this class lies in region consistent with simulations ($0.1 \lesssim \lambda_{R_e} \lesssim 0.3$) (T. Naab et al. 2014, Class D in their fig. 7). This feature also resembles the Class 2 galaxies in (J. de Sande et al. 2017, see their Fig. 14). The galaxies with inner anticorrelated discs are rounder and rotate faster than non-correlated galaxies. This also indicates that this category of galaxies is distinct on its own.

In Fig. 17, we show the location of the fast rotators in the mass-size plane coloured by their kinematic classes based on high-order moments. The stellar masses used here are twice the stellar masses calculated within the elliptical half-light isophotes, taken from the catalogue of S. Lu et al. (2023) under the keyword `'Mstar_Re'`. The ages and metallicities used in Figs 18 and 19 are the SDSS $r-$band (C. Stoughton et al. 2002) luminosity-weighted average value within the half-light isophote under keyword `'LW_Age_Re'` and `'LW_Metal_Re'`, also from S. Lu et al. (2023). The selection criteria in Section 2.2 ($\langle\sigma\rangle_e \gtrsim 140$ km s^{-1}) makes our sample dominated by massive galaxies. As confirmed by the Kolmogorov–Smirnov (KS) test (A. N. Kolmogorov 1933; N. V. Smirnov 1939; F. J. Massey 1951) with a p-value of $\sim 10^{-6}$, the diagram shows that non-correlated galaxies are larger and more massive, while the galaxies with inner anticorrelated discs are smaller and less massive compared with common anticorrelated fast rotators.

In Figs 18 and 19, although there are no significant differences in metallicity among the three types of galaxies, the inner disc galaxies are slightly younger compared to the other two classes as indicated by a KS test with a p-value of 0.012. The star formation rates of the smaller-mass galaxies in inner disc galaxies are similar to those of the other two classes, resulting in higher specific star formation

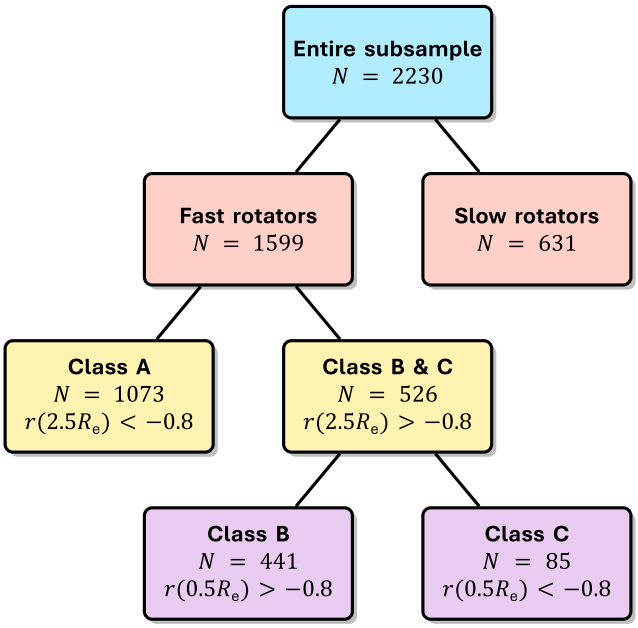

Figure 15. Galaxies are first classified as slow or fast rotators based on their kinematic morphology. Slow rotators do not show significant V/σ–h_3 correlations and are not further subdivided. Fast rotators are further divided into three classes according to the Pearson correlation coefficients between V/σ and h_3: Class A ($r(2.5R_e) < -0.8$), Class B ($r(2.5R_e) > -0.8$ and $r(2.5R_e) > -0.8$), and Class C ($r(2.5R_e) > -0.8$ but $r(0.5R_e) < -0.8$).

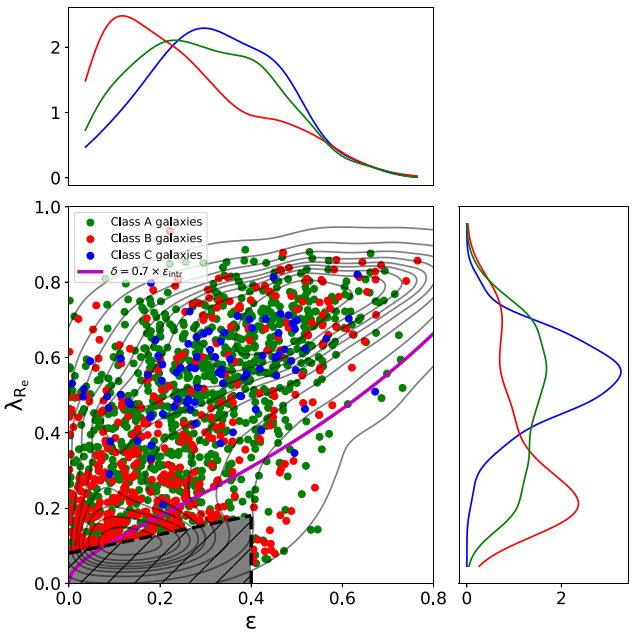

Figure 16. The λ_R-parameter versus projected edge-on ellipticities at R_e. The galaxies are colour coded by their class: green for anticorrelated galaxies, red for non-correlated galaxies and blue for galaxies with inner anticorrelated discs. The solid magenta line is the theoretical prediction for the edge-on view of axisymmetric galaxies with $\beta_z = 0.7 \times \varepsilon_{intr}$ (M. Cappellari et al. 2007, fig. 9). The contour lines are kernel density estimate of all the galaxies in MaNGA. The shaded area are for slow rotators.

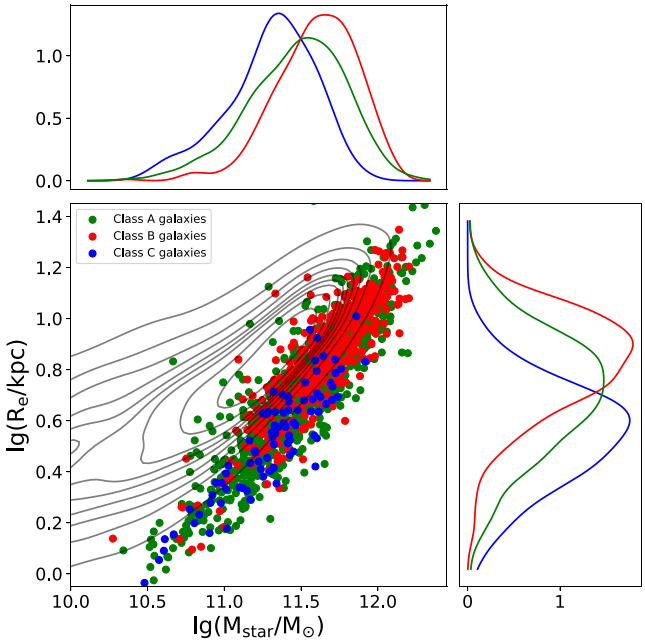

Figure 17. The stellar mass versus effective radius of our galaxy samples. The galaxies are colour coded by their classes as in Fig. 16. The contour lines are kernel density estimate of all the galaxies in MaNGA.

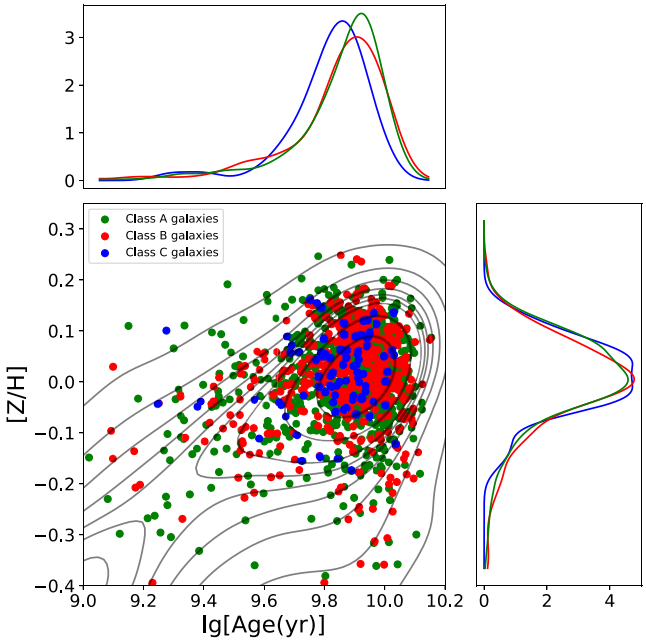

Figure 18. The age vs. metallicity of our galaxy samples. The galaxies are colour coded by their classes as in Fig. 16. The contour lines are kernel density estimate of all the galaxies in MaNGA.

rates. Further investigation of the age and dust maps finds that 42 out of 85 galaxies' inner discs are younger, as shown in the top two galaxies in Fig. 20. There is no clear evidence of a younger stellar population at the centre of the remaining galaxies. However, we find dust lanes in 11 galaxies, indicating possible recent star-forming activities.

The inner, anticorrelated h_3 disc indicates the formation of a kinematically decoupled core structure (e.g. M. Bois et al. 2011;

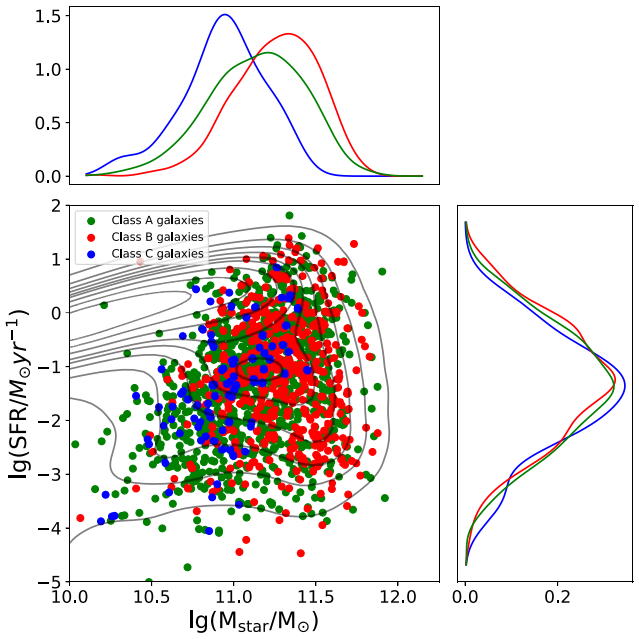

Figure 19. The stellar mass versus star formation rate of our galaxy samples. The galaxies are colour coded by their classes as in Fig. 16. The contour lines are kernel density estimate of all the galaxies in MaNGA.

A. Rantala et al. 2019; D. A. Gadotti et al. 2020). For some galaxies, the formation of the discs was more recent, so we can observe a younger stellar population. For other galaxies, the formation time of a young inner-disc is not seen in their ages but is revealed by the presence of dust in 11 galaxies.

4.5 Impact of galaxy bars and mergers

Multiple kinematic components such as a bar or strong merger signatures can blend correlations and anticorrelations. Accordingly, we aim to investigate specifically how galaxy bars and mergers affect the correlation between h_3 and V/σ.

4.5.1 Impact of galaxy bars on h_3

Previous *N*-body simulations of barred galaxies show a weak positive correlation between h_3 and V/σ in the bar region (M. Bureau & E. Athanassoula 2005; F. Iannuzzi & E. Athanassoula 2015; Z.-Y. Li et al. 2018). We identify barred galaxies in our sample using the catalogue of barred galaxies in MaNGA by H. Domínguez Sánchez et al. (2022). We adopt the recommended classification scheme in the article. The barred galaxies are those with keywords `'P_bar'` greater than 0.8 (section 3.1 of H. Domínguez Sánchez et al. 2022). There are 121 barred galaxies in our sample of 1599 fast rotators. We build a control sample by selecting the closest unbarred fast rotator for every barred galaxy in the mass–size plane of Fig. 17. We show the local $h_3 - V/\sigma$ relation for all data points in barred galaxies and the control sample in Fig. 21. The negative correlation is weakened and becomes more vertical.

Overall, barred galaxies show a steeper relation in the h_3 versus V/σ diagram. We do not observe a statistically significant positive correlation predicted by simulations in barred galaxies. This may be due to the rotation-dominated nuclear discs in the central regions of barred galaxies. Z.-Y. Li et al. (2018) points out that additional nuclear substructures in the central region of a bar could overwhelm the weak positive correlation predicted by simulation. D. A. Gadotti et al. (2020) discovers the presence of nuclear discs in 19 galaxies out of 21 nearby massive barred galaxies. The rotation-supported nuclear discs show a significant anticorrelation between h_3 and V/σ in the galaxy central region ($\sim$ 1kpc) (D. A. Gadotti et al. 2020, see their table 2 and Appendix A). In simulation, positive correlations exist on spatial scales around 4 kpc (Z.-Y. Li et al. 2018, their section 3). The presence of nuclear discs in the majority of barred galaxies may reduce our ability to detect positive correlations. At the median physical resolutions of 1.37 and 2.5 kpc for the MaNGA Primary and Secondary samples (D. A. Wake et al. 2017), the positive h_3–V/σ correlation induced by bars can be easily blended with the anticorrelation signal of the disc, resulting in a non-correlation feature. All of these could be reasons for the discrepancies between our observations and the simulation results.

4.5.2 Impact of mergers on h_3

We identify galaxy pairs and mergers using the catalogue of MaNGA galaxy mergers by J. M. Comerford et al. (2024). We adopt their recommended classification scheme. Following the practice recommended in R. Nevin et al. (2023), the galaxy mergers are those with keywords `'p_merg_stat_50_major_merger'` or `'p_merg_stat_50_minor_merger'` greater than 0.5. This results in 561 galaxies classified pairs or mergers in our sample of 1599 fast rotators. Similarly, we build a control sample by selecting the closest non-merging fast rotator for every merger in the mass–size plane (Fig. 17).

Fig. 22 shows the local $h_3 - V/\sigma$ relation for all data points in mergers and the control sample. The anticorrelation still maintains but becomes weaker in pairs and mergers. In the centre where the bins are most densely concentrated, mergers exhibit a more irregular distribution in the $h_3 - V/\sigma$ diagram. The result is in line with expectations. J. de Sande et al. (2017) also finds that fast rotators showing a weaker anticorrelation (Class 5 in their classification) are more likely disturbed galaxies. This may originate from the complex dynamical processes and multiple kinematic components in galaxy pairs and mergers. At the spatial resolution of MaNGA and SAMI, these components cannot be fully resolved, resulting in these galaxies exhibiting a weaker anticorrelation.

5 DISCUSSION

This section interprets our kinematic classifications by comparing them with cosmological simulations, primarily the hydrodynamical zoom-in simulations of T. Naab et al. (2014). This comparison allows us to connect the observed kinematic features of galaxies in our sample to their likely formation and merger histories.

A significant fraction of our sample – approximately two-thirds of all fast rotators – are classified as having anticorrelated kinematics. These galaxies align well with the 'Class A and B' fast rotators in T. Naab et al. (2014). Key shared features include a distinct h_3–V/σ anticorrelation and the *V*-shaped structure in the h_4– V/σ plane (as seen in our Figs 11 and 9 of their study). This strong correspondence supports the prevailing theory that most fast-rotating galaxies are the products of gas-rich mergers, a scenario corroborated by multiple studies (T. Naab et al. 2006a, 2014; J. de Sande et al. 2017).

Conversely, our non-correlated fast rotators exhibit kinematics consistent with the 'Class D' galaxies from T. Naab et al. (2014), characterized by angular momentum values in the range $0.1 \lesssim \lambda_{R_e} \lesssim$

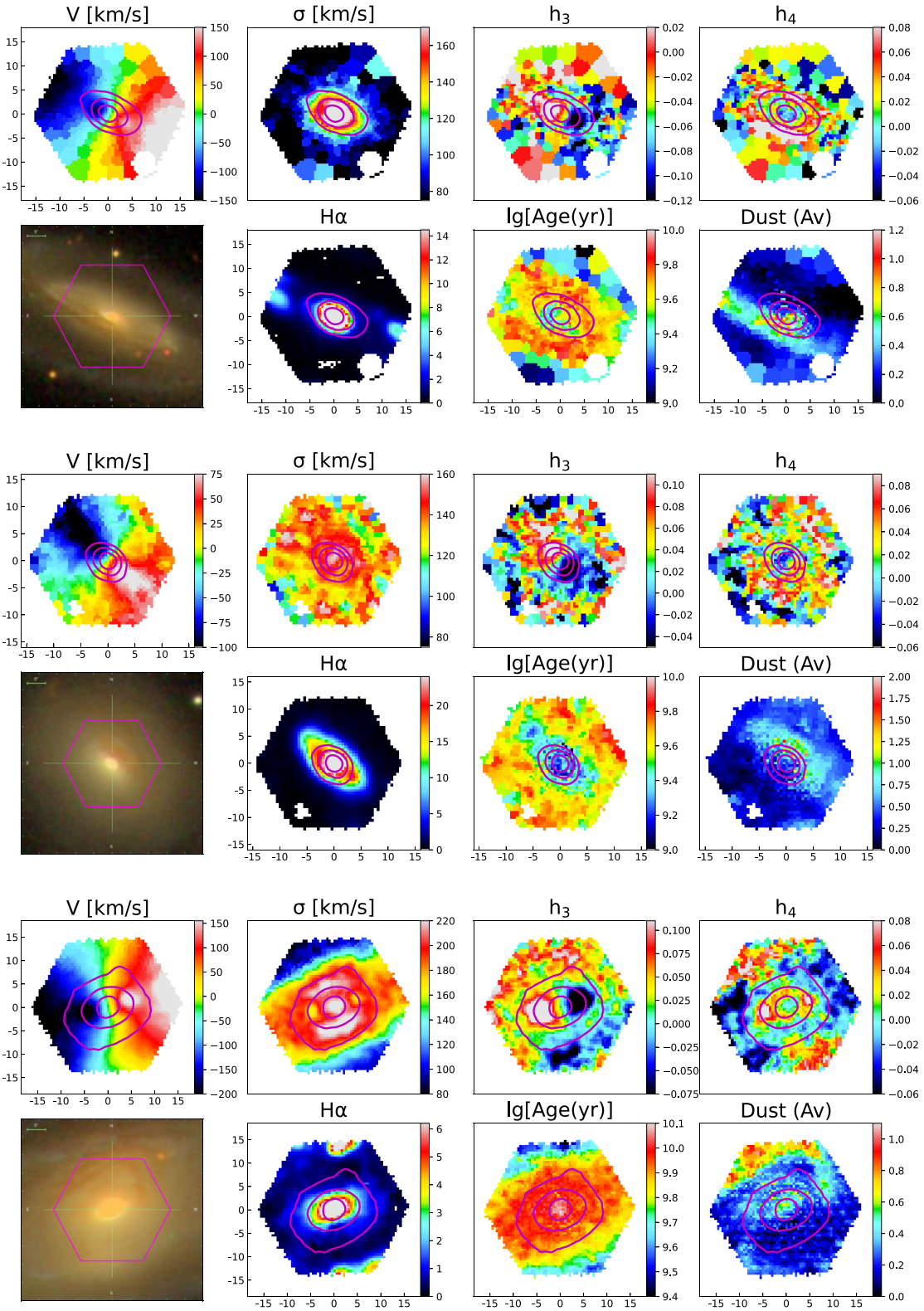

Figure 20. Examples of three fast rotators with anticorrelated $h_3 - V/\sigma$ relation (MaNGA-ID: 1–38101, 1–90190, 1–605551 from top to bottom). The top rows are two-dimensional stellar kinematics maps for three galaxies. The solid magenta contour lines represent the surface brightness. The left panels in the bottom rows show the galaxy images from MaNGA. The star-forming activities in each galaxy are represented by the relative flux of the Hα emission line in the second left panel. The age and dust maps are shown in the right two panels. The tick labels on the spatial axes are in units of arcseconds.

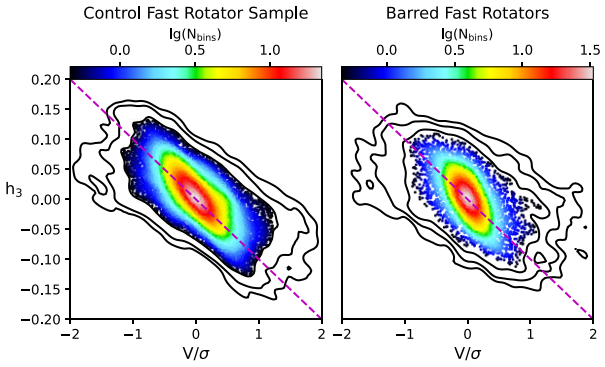

Figure 21. Local $h_3 - V/\sigma$ relation for all bins of barred galaxies (right) and control fast rotator sample (left). The panels are colour-coded as in Fig. 8. The dashed magenta lines with a slope of −0.1 plotted in both panels for references, which is approximately the slope of the linear fit in R. Bender et al. (1994).

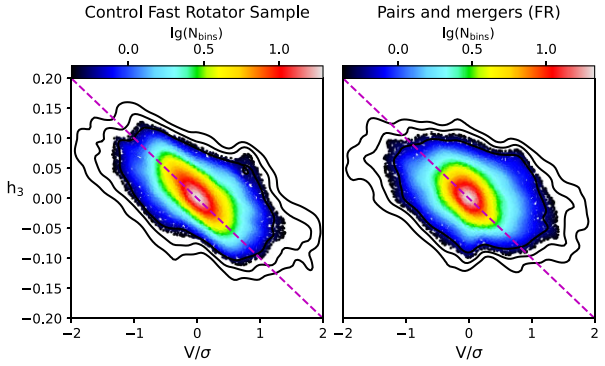

Figure 22. Local $h_3 - V/\sigma$ relation for all bins of fast rotator mergers (right) and control fast rotator sample (left). The panels are colour-coded as in Fig. 8. The dashed magenta lines with a slope of −0.1 plotted in both panels for references, which is approximately the slope of the linear fit in R. Bender et al. (1994).

0.3. The defining feature of this class is the absence of a clear anticorrelation between h_3 and V/σ, which suggests they lack significant embedded, disc-like components. Cosmological simulations trace the origin of such galaxies to recent, gas-poor major mergers (T. Naab et al. 2006a, b; R. Jesseit et al. 2007).

When comparing the population statistics, T. Naab et al. (2014) predict that non-correlated fast rotators (Class D) should constitute about 31 per cent (5/16) of the fast-rotator population. In our sample, the observed ratio of non-correlated (our Class B) to anticorrelated (our Class A) galaxies is 41 per cent (441/1073), a fraction somewhat higher than expected.

It is crucial, however, to approach this quantitative comparison with caution. Cosmological simulations are not complete, volume-limited samples; by design, they are often biased towards massive galaxies, due to numerical resolution issues, and our subsample is by design focused on high-dispersion galaxies, for which we can measure higher-order moments. Given that achieving perfectly matched samples between observations and simulations is difficult, a direct comparison of population fractions may not be meaningful. The difference we find could therefore reflect intrinsic differences between the samples as much as a physical insight.

Beyond this fundamental limitation, another possible reason for the difference may be that our global classification metric oversimplifies the kinematics of galaxies with complex internal structures. For instance, systems with prominent bars or recent merger signatures can host multiple, co-spatial kinematic components where local anticorrelations and positive correlations coexist (e.g. D. A. Gadotti et al. 2020). The global Pearson coefficient in such cases could be suppressed, leading to a misclassification of these structurally complex galaxies as simple non-correlated rotators.

Furthermore, our identification of Class C galaxies – those with strong central anticorrelations indicative of kinematically distinct cores – is highly sensitive to spatial resolution. It is plausible that in many galaxies, these compact central structures are blurred by seeing effects and blended with the larger-scale disc kinematics, making them difficult to detect. This would lead to an undercounting of Class C systems. To have an idea of the effect one can compare the fraction of nuclear discs in the ATLAS^{3D} survey (D. Krajnović et al. 2011) with the much lower fraction in the lower-resolution MaNGA survey (M. T. Graham et al. 2018). Future observations with high-resolution integral-field spectrographs, such as MUSE, will be crucial for resolving these ambiguities. By resolving fine-grained kinematic details, we can refine the link between the high-order kinematic signatures we observe today and the rich assembly histories of galaxies seen in simulations.

6 CONCLUSION

In this paper, we have selected a subsample of 2230 galaxies with regular kinematic maps and well-resolved LOSVD (i.e. $\sigma_e \gtrsim 140$ km s^{-1}) from the MaNGA survey to study high-order stellar kinematic signatures. One of the goals of this paper is to describe the extraction of the stellar kinematics, which will be used in a subsequent paper for dynamical modelling using the M. Schwarzschild (1979) method. Following K. B. Westfall et al. (2019), we constructed new stellar templates of 54 spectra based on the MaStar stellar library. These new templates minimize the problems of template mismatch and undersampling, reducing systemic error when fitting higher-order terms.

We describe our measurements of stellar kinematics in the MaNGA data using PPXF (M. Cappellari 2023). We show that systemic error due to the combination of pixel spectra with different initial velocities by Voronoi binning has a completely negligible effect on the Gauss-Hermite moments h_3 and h_4 (R. P. der Marel & M. Franx 1993). Following the classical procedure, we use the spin parameter (λ_{R_e}) (E. Emsellem et al. 2007) and ellipticity (ε) to separate galaxies into fast and slow rotators. We confirm the classical anticorrelation of h_3 and V/σ for fast rotators (R. Bender et al. 1994). However, we find no clear statistical correlation between h_3 and V/σ in slow rotators.

Fast rotators are further classified into subclasses based on the Pearson correlation coefficient between h_3 and V/σ. We identify three classes with different high-order stellar kinematic signatures: 1073 fast rotators show a distinct anticorrelation in the h_3–V/σ diagram within the $2.5R_e$ field of view. Among the remainder, 85 fast rotators have an anticorrelated h_3 inner disc within around $0.5R_e$. Further analyses of their stellar populations find that half of these have young star-forming discs. Additionally, 441 fast rotators do not show an h_3 versus V/σ anticorrelation. Detailed morphological inspection reveals that many of these galaxies are disturbed, showing barred or merging signatures.

We compare our high-order kinematic classes to the hydrodynamical cosmological zoom-in simulations of T. Naab et al. (2014) and the observation catalogue from J. de Sande et al. (2017). Following their works, our classification focused primarily on the h_3 signatures. Two-

thirds of the fast rotators in our sample show a strong anticorrelation between h_3 and V/σ corresponding to Class 3−4 in J. de Sande et al. (2017). Our non-correlated fast rotators closely resemble the features of Class 2 galaxies in their work with smaller spin parameters (J. de Sande et al. 2017). We also confirm the finding of the *V*-shaped structure in h_4 versus V/σ diagram in simulation (T. Naab et al. 2014, see their Fig. 9). Interesting patterns like this warrant further study.

Our large catalogue of galaxies with reliable h_3 and h_4 measurements will be useful for further studies of stellar dynamics and galaxy formation. The kinematics, including h_3 and h_4, will be used to constrain dynamical models in a subsequent paper to understand the dynamical structure and formation history of galaxies.

ACKNOWLEDGEMENTS

We thank the referee for helpful comments that improved the paper. This work (for YF and SM) is partly supported by the National Nature Science Foundation of China (Grant No. 11821303) and by the Tsinghua University Initiative Scientific Research Program ID 2019Z07L02017. We also acknowledge the science research grants from the China Manned Space Project with No. CMS-CSST-2021-A11.

Funding for the SDSS-IV has been provided by the Alfred P. Sloan Foundation, the U.S. Department of Energy Office of Science, and the Participating Institutions.

SDSS-IV acknowledges support and resources from the Center for High Performance Computing at the University of Utah. The SDSS web site is www.sdss.org.

SDSS-IV is managed by the Astrophysical Research Consortium for the Participating Institutions of the SDSS Collaboration including the Brazilian Participation Group, the Carnegie Institution for Science, Carnegie Mellon University, Center for Astrophysics| Harvard & Smithsonian, the Chilean Participation Group, the French Participation Group, Instituto de Astrofísica de Canarias, The Johns Hopkins University, Kavli Institute for the Physics and Mathematics of the Universe (IPMU) University of Tokyo, the Korean Participation Group, Lawrence Berkeley National Laboratory, Leibniz Institut für Astrophysik Potsdam (AIP), Max-Planck-Institut für Astronomie (MPIA Heidelberg), Max-Planck-Institut für Astrophysik (MPA Garching), Max-Planck-Institut für Extraterrestrische Physik (MPE), National Astronomical Observatories of China, New Mexico State University, New York University, University of Notre Dame, Observatário Nacional/MCTI, The Ohio State University, Pennsylvania State University, Shanghai Astronomical Observatory, United Kingdom Participation Group, Universidad Nacional Autónoma de México, University of Arizona, University of Colorado Boulder, University of Oxford, University of Portsmouth, University of Utah, University of Virginia, University of Washington, University of Wisconsin, Vanderbilt University, and Yale University.

DATA AVAILABILITY

The data underlying this article are available in the article and in its online supplementary material. The stellar templates and kinematics are publicly available on the website (https://github.com/Fuyq42/MaNGA_High_Order_stellar_kinematic).

REFERENCES

Abdurro'uf et al., 2022, ApJS, 259, 35
Belfiore F. et al., 2019, AJ, 158, 160
Bender R., Saglia R. P., Gerhard O. E., 1994, MNRAS, 269, 785
Binney J., Mamon G. A., 1982, MNRAS, 200, 361
Bois M. et al., 2011, MNRAS, 416, 1654
Bryant J. J. et al., 2015, MNRAS, 447, 2857
Bundy K. et al., 2015, ApJ, 798, 7
Bureau M., Athanassoula E., 2005, ApJ, 626, 159
Cappellari M., 2008, MNRAS, 390, 71
Cappellari M., 2016, ARA&A, 54, 597
Cappellari M., 2017, MNRAS, 466, 798
Cappellari M., 2020, MNRAS, 494, 4819
Cappellari M., 2023, MNRAS, 526, 3273
Cappellari M., in Mandel I. , ed. Elsevier,Radarweg 29, 1043 NX Amsterdam, Netherlands, 2026, in Encyclopedia of Astrophysics. p. 122, https://ui.adsabs.harvard.edu/abs/2026enap....4..122C, (Accessed 27 Oct. 2025)
Cappellari M., Copin Y., 2003, MNRAS, 342, 345
Cappellari M., Emsellem E., 2004, PASP, 116, 138
Cappellari M. et al., 2007, MNRAS, 379, 418
Cappellari M. et al., 2011, MNRAS, 413, 813
Chung A., Bureau M., 2004, AJ, 127, 3192
Cole D. R., Debattista V. P., Erwin P., Earp S. W. F., Roškar R., 2014, MNRAS, 445, 3352
Comerford J. M. et al., 2024, ApJ, 963, 53
D'Eugenio F. et al., 2023a, MNRAS, 525, 2765
D'Eugenio F. et al., 2023b, MNRAS, 525, 2789
Debattista V. P., Carollo C. M., Mayer L., Moore B., 2005, ApJ, 628, 678
Domínguez Sánchez H., Margalef B., Bernardi M., Huertas-Company M., 2022, MNRAS, 509, 4024
Drory N. et al., 2015, AJ, 149, 77
Emsellem E. et al., 2007, MNRAS, 379, 401
Emsellem E. et al., 2011, MNRAS, 414, 888
Fraser-McKelvie A. et al., 2025, A&A, 700, A237
Gadotti D. A. et al., 2020, A&A, 643, A14
Gerhard O., Jeske G., Saglia R. P., Bender R., 1998, MNRAS, 295, 197
Gerhard O. E., 1993, MNRAS, 265, 213
Graham M. T. et al., 2018, MNRAS, 477, 4711
Hill L. et al., 2022, MNRAS, 509, 4308
Iannuzzi F., Athanassoula E., 2015, MNRAS, 450, 2514
Jain A. K., Murty M. N., Flynn P. J., 1999, ACM Comput. Surv., 31, 264
Jesseit R., Naab T., Burkert A., 2005, MNRAS, 360, 1185
Jesseit R., Naab T., Peletier R. F., Burkert A., 2007, MNRAS, 376, 997
Kolmogorov A. N., 1933, Giornale dell'Istituto Italiano degli Attuari, 4, 83
Krajnović D., Cappellari M., de Zeeuw P. T., Copin Y., 2006, MNRAS, 366, 787
Krajnović D. et al., 2008, MNRAS, 390, 93
Krajnović D. et al., 2011, MNRAS, 414, 2923
Krajnović D. et al., 2013, MNRAS, 432, 1768
Law D. R. et al., 2016, AJ, 152, 83
Law D. R. et al., 2021, ApJ, 915, 35
Li Z.-Y., Shen J., Bureau M., Zhou Y., Du M., Debattista Victor P., 2018, ApJ, 854, 65
Loubser S. I., Lagos P., Babul A., O'Sullivan E., Jung S. L., Olivares V., Kolokythas K., 2022, MNRAS, 515, 1104
Lu S., Zhu K., Cappellari M., Li R., Mao S., Xu D., 2023, MNRAS, 526, 1022
van der Marel R. P., Rix H. W., Carter D., Franx M., White S. D. M., de Zeeuw T., 1994, MNRAS, 268, 521
Massey F. J., 1951, J. Am. Stat. Assoc., 46, 68
Naab T., Jesseit R., Burkert A., 2006a, MNRAS, 372, 839
Naab T., Khochfar S., Burkert A., 2006b, ApJ, 636, L81
Naab T. et al., 2014, MNRAS, 444, 3357
Nevin R., Blecha L., Comerford J., Simon J., Terrazas B. A., Barrows R. S., Vázquez-Mata J. A., 2023, MNRAS, 522, 1
Rantala A., Johansson P. H., Naab T., Thomas J., Frigo M., 2019, ApJ, 872, L17
Sánchez S. F. et al., 2012, A&A, 538, A8
Schwarzschild M., 1979, ApJ, 232, 236
Smirnov N. V., 1939, Bulletin of Moscow University, 2, 3

Stoughton C. et al., 2002, AJ, 123, 485
Thomas J., Saglia R. P., Bender R., Thomas D., Gebhardt K., Magorrian J., Corsini E. M., Wegner G., 2007, MNRAS, 382, 657
Vazdekis A., Sánchez-Blázquez P., Falcón-Barroso J., Cenarro A. J., Beasley M. A., Cardiel N., Gorgas J., Peletier R. F., 2010, MNRAS, 404, 1639
Vazdekis A. et al., 2015, MNRAS, 449, 1177
Wake D. A. et al., 2017, AJ, 154, 86
Wang Z., Sharma S., Hayden M. R., van de Sande J., Bland-Hawthorn J., Vaughan S., Martig M., Pinna F., 2024, MNRAS, 534, 1175
Westfall K. B. et al., 2019, AJ, 158, 231
Yan R. et al., 2019, ApJ, 883, 175
Zakharova D., Tikhonenko I. S., Sotnikova N. Y., Smirnov A. A., 2023, MNRAS, 525, 6112
Zhu K., Lu S., Cappellari M., Li R., Mao S., Gao L., 2023, MNRAS, 522, 6326
Zhu K., Lu S., Cappellari M., Li R., Mao S., Gao L., Ge J., 2024, MNRAS, 527, 706
van de Sande J. et al., 2017, ApJ, 835, 104
van der Marel R. P., Franx M., 1993, ApJ, 407, 525

SUPPORTING INFORMATION

Supplementary data are available at *MNRAS* online.
Table 1 : The catalogue of Pearson coefficient within 2.5Re and 0.5Re isophote for fast rotators in our sample.
Please note: Oxford University Press is not responsible for the content or functionality of any supporting materials supplied by the authors. Any queries (other than missing material) should be directed to the corresponding author for the article.

APPENDIX A: A COMPARISON TO THE VELOCITY AND DISPERSION VALUES PROVIDED BY THE MANGA DAP

In Fig. A1, we present a comparison of the velocity and velocity dispersion measurements with those of the data analysis pipeline (K. B. Westfall et al. 2019) of the MaNGA survey.

The DAP measurements is based on a Gaussian LOSVD. If the LOSVD is purely Gaussian, the Gaussian measurements and Gauss–Hermite parameters are identical. However, for a non-Gaussian LOSVD, the Gauss–Hermite parametrization, accounting for the skewness and kurtosis of the distribution, leads to deviations in the measured velocity $V_{\rm GH}$ and velocity dispersion $\sigma_{\rm GH}$ from those of a purely Gaussian LOSVD, denoted as $V_{\rm Gauss}$ and $\sigma_{\rm Gauss}$. Furthermore, the best-estimates of the true LOSVD moments can be calculated by equations A1 and A2 (equation 18 in R. P. der Marel & M. Franx 1993). A useful comparison can be seen in fig. 3 of J. de Sande et al. (2017).

$$V_{\rm Gauss} \approx V_{\rm GH} + \sqrt{3}\,\sigma_{\rm GH}\,h_3, \tag{A1}$$

$$\sigma_{\rm Gauss} \approx \sigma_{\rm GH}\left(1 + \sqrt{6}\,h_4\right). \tag{A2}$$

To account for differences in binning schemes, we adopt the Voronoi binning approach described in this paper. The velocity and dispersion values from the DAP MAPS files (section 12.1 in K. B. Westfall et al. 2019) are combined within each bin with flux-weighted averaging. As can be seen, our values agree well with the expected values from the DAP.

APPENDIX B: KINEMATIC PROPERTIES INCLUDED IN THE CATALOGUE

We present the data model of this catalogue in Table B1, which lists the dynamical properties derived from the analysis described in this paper.

We choose to include two sets of kinematics in our catalogue: PPXF fits using a pure Gaussian LOSVD as well as PPXF fits using a Gauss–Hermite LOSVD out to h_4. We do this because there are some applications, such as dynamical modelling, where it may be preferable to only fit a Gaussian LOSVD rather than include higher order moments. This is because the wings of the LOSVD are not as well constrained by the data as the central Gaussian peak. In cases where there is template mismatch or the underlying kinematics are not well approximated by the lowest order terms in the Gauss–Hermite series, this can lead to residuals which may bias the results. This is especially true for Jeans Modelling, which uses the second velocity moment, given by

$$V_{\rm rms} \equiv \sqrt{V^2 + \sigma^2} \tag{B1}$$

where V and σ are the mean and standard deviation of the LOSVD. For a pure Gaussian LOSVD these are just the parameters V and σ of the Gaussian, but for a Gauss–Hermite LOSVD these must be calculated from the shape of the LOSVD. In practice, when only considering moments up to h_4, these are well approximated by equations A1 and A2.

On top of issues related to data quality, an important complicating factor is that, as shown in Simon et al. (in preparation) measurements of the second moment do not uniformly improve when including higher order terms in the Gauss–Hermite series. This is because, while including higher order moments will, in the idealized case, improve the overall fit to the LOSVD, this is primarily due to the addition of smaller contributions to the LOSVD wings. These contributions can induce some small residuals which the second moment is sensitive to. For this reason, we provide both Gaussian-only and Gauss–Hermite fits, allowing catalogue users to select the version most appropriate to their studies.

This paper has been typeset from a TEX/LATEX file prepared by the author.

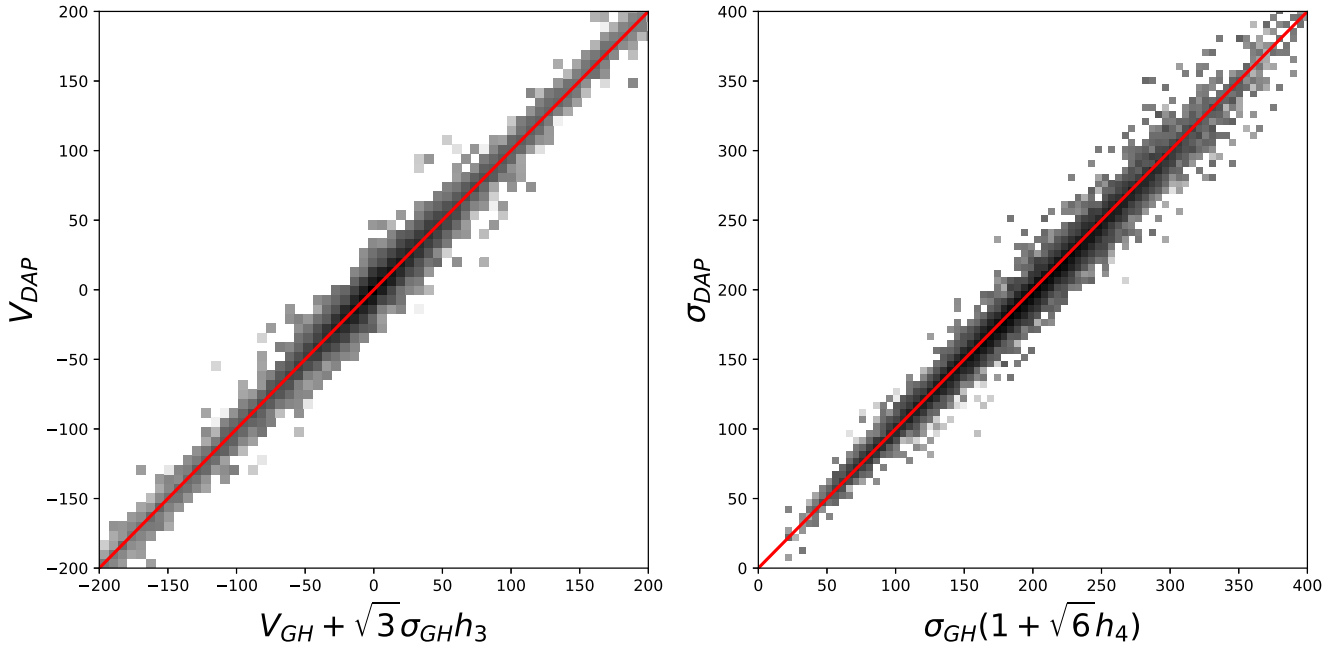

Figure A1. In the panels, we show the comparison between best-fitted 4-moments LOSVD present in this paper and the best-fitted Gaussian moments in DAP (K. B. Westfall et al. 2019). The grey scale shows the density of spaxels. The solid red lines show the equality line.

Table B1. Kinematic moments for each galaxy. For each galaxy, the Header Data Unit (HDU) in which it is stored, the name, its units, and a brief description are presented. The properties with prefix 'DAP' are taken from the DAP MAPS file (section 12.1 in K. B. Westfall et al. 2019).

HDU (1)	Name (2)	Dimensions (3)	Units (4)	Description (5)
0	Primary			Empty primary header
1	DAP_SPX_SKYCOO	(N, N,2)	arcsec	Sky-right offsets +x toward +RA and +y toward +DEC—of each spaxel from the galaxy centre. Same as the `'SPX_SKYCOO'` in corresponding MAPS file.
2	DAP_SPX_MFLUX	(N, N)	10^{-17}erg s^{-1} cm^{-2} Å^{-1} spaxel^{-1}	g-band-weighted mean flux, not corrected for Galactic extinction or internal attenuation. Same as the `'SPX_MFLUX'` in corresponding MAPS file.
3	BINID	(N, N)		Numerical ID for spatial bins binned to S/N = 30
4	Stellar_Vel_Gauss	(N, N)	km s^{-1}	Gaussian line-of-sight stellar velocity derived with moments = 2.
5	Stellar_Vel_Ivar_Gauss	(N, N)		Inverse variance in STELLAR_VEL_Gauss.
6	Stellar_Sigma_Gauss	(N, N)	km s^{-1}	Gaussian line-of-sight stellar velocity dispersion derived with moments = 2.
7	Stellar_Sigma_ivar_Gauss	(N, N)		Inverse variance in Stellar_Sigma_Gauss
8	Stellar_Vel_GH	(N, N)	km s^{-1}	Line-of-sight stellar velocity derived from fitting four kinematic moments (V, σ, h_3, h_4) with moments = 4.
9	Stellar_Vel_Ivar_GH	(N, N)		Inverse variance in STELLAR_VEL_GH.
10	Stellar_Sigma_GH	(N, N)	km s^{-1}	Line-of-sight stellar velocity dispersion derived from fitting four kinematic moments (V, σ, h_3, h_4) with moments = 4.
11	Stellar_Sigma_ivar_GH	(N, N)		Inverse variance in Stellar_Sigma_GH
12	Stellar_h3_GH	(N, N)		Line-of-sight stellar h_3 derived from fitting four kinematic moments (V, σ, h_3, h_4) with moments = 4.
13	Stellar_h3_ivar_GH	(N, N)		Inverse variance in Stellar_h3_GH
14	Stellar_h4_GH	(N, N)		Line-of-sight stellar h_4 derived from fitting four kinematic moments (V, σ, h_3, h_4) with moments = 4.
15	Stellar_h4_ivar_GH	(N, N)		Inverse variance in Stellar_h4_GH